Bioactive Materials 22 (2023) 112–126

Contents lists available at ScienceDirect

Bioactive Materials

journal homepage: www.keaipublishing.com/en/journals/bioactive-materials

Upconverting nanoparticle-containing erythrocyte-sized hemoglobin microgels that generate heat, oxygen and reactive oxygen species for suppressing hypoxic tumors

Hanju Kim [a], Johyun Yoon [a], Hwang Kyung Kim [a], Woo Tak Lee [a], Nguyen Thi Nguyen [a], Xuan Thien Le [a], Eun-Hee Lee [b], Eun Seong Lee [c], Kyung Taek Oh [d], Han-Gon Choi [e], Yu Seok Youn [a,*]

[a] School of Pharmacy, Sungkyunkwan University, 2066 Seobu-ro, Jangan-gu, Suwon, Gyeonggi-do, 16419, Republic of Korea
[b] College of Pharmacy, Korea University, 2511 Sejong-ro, Sejong, 30019, Republic of Korea
[c] Department of Biotechnology and Department of Biomedical-Chemical Engineering, the Catholic University of Korea, 43 Jibong-ro, Bucheon-si, Gyeonggi-do, 14662, Republic of Korea
[d] College of Pharmacy, Chung-Ang University, 84 Heukseok-ro, Dongjak-gu, Seoul, 06974, Republic of Korea
[e] College of Pharmacy, Hanyang University, 55, Hanyangdaehak-ro, Sangnok-gu, Ansan, 15588, Republic of Korea

ARTICLE INFO

Keywords:
Hemoglobin microgel
Upconversion
Photothermal therapy
Photodynamic therapy
Hypoxic tumors
Oxygen-generation

ABSTRACT

Inspired by erythrocytes that contain oxygen-carrying hemoglobin (Hb) and that exhibit photo-driven activity, we introduce homogenous-sized erythrocyte-like Hb microgel (μGel) systems (5–6 μm) that can (i) emit heat, (ii) supply oxygen, and (iii) generate reactive oxygen species (ROS; $^1O_2$) in response to near-infrared (NIR) laser irradiation. Hb μGels consist of Hb, bovine serum albumin (BSA), chlorin e6 (Ce6) and erbium@lutetium upconverting nanoparticles (UCNPs; ~35 nm) that effectively convert 808 nm NIR light to 660 nm visible light. These Hb μGels are capable of releasing oxygen to help generate sufficient reactive oxygen species ($^1O_2$) from UCNPs/Ce6 under severely hypoxic condition upon NIR stimulation for efficient photodynamic activity. Moreover, the Hb μGels emit heat and increase surface temperature due to NIR light absorption by heme (iron protoporphyrin IX) and display photothermal activity. By changing the Hb/UCNP/Ce6 ratio and controlling the amount of NIR laser irradiation, it is possible to formulate bespoke Hb μGels with either photothermal or photodynamic activity or both in the context of combined therapeutic effect. These Hb μGels effectively suppress highly hypoxic 4T1 cell spheroid growth and xenograft mice tumors *in vivo*.

1. Introduction

Hemoglobin (Hb) is a natural tetrameric protein present in erythrocytes and comprising two α and two β polypeptide subunits that binds to oxygen [1]. The high oxygen-binding capacity of Hb has resulted in the development of many nano- or micro-scale Hb-based oxygen carriers (HBOCs) to supply oxygen as a blood substitute and mimic erythrocyte function [2]. Chemically-modified Hb conjugates (cross-linked, PEGylated, polymerized Hb, etc.) [3–6] and Hb-encapsulating particles (Hb-coated/containing liposomes/nanogels, microspheres, etc.) have shown high oxygen-supply potential. Oxyglobin™ (Biopure, Inc., USA), a glutaraldehyde-crosslinked bovine Hb, was approved in Europe and USA for veterinary use [5]. Moreover, Hb has much higher O_2-binding affinity than fluorocarbon-based oxygen carriers (FBOCs) like Fluosol-DA™, a 20% PFC formula [7], and is also known to generate hydroxy radicals (•OH) via the Fenton reaction during autoxidation [8,9]. In addition, attempts have been made to mimic the shape, structure, and functions of Hb-containing erythrocytes to develop new biological templates [10–12]. Likewise, Hb is viewed as one of the most versatile materials for oxygen therapeutics.

Tumor hypoxia, which results from structural abnormalities of the tumor vasculature, is considered a critical hurdle in cancer therapy. Solid tumors contain numerous hypoxic regions because their vasculature is unable to supply sufficient oxygen to each cell [13,14]. The

Peer review under responsibility of KeAi Communications Co., Ltd.
* Corresponding author.
E-mail address: ysyoun@skku.edu (Y.S. Youn).

https://doi.org/10.1016/j.bioactmat.2022.09.020
Received 21 June 2022; Received in revised form 16 September 2022; Accepted 19 September 2022

reduced oxygen level in hypoxic tumors impairs the therapeutic efficiency of chemotherapeutics, radioactive medicines, and photosensitizing agents that require oxygen for activity. Oxygen level of severe hypoxic tumors has been measured as less than 5 mmHg (<0.7%) compared to the 30–52 mmHg (3.9–6.8%) oxygen level of normal tissues [15]. Hence, sufficient oxygenation is essential for treating hypoxic tumors, and many strategies to elevate oxygen level have been investigated to overcome hypoxia-induced resistance to cancer treatment [16–23].

Photodynamic therapy (PDT) is a highly effective tumor treatment. Photosensitizing agents (PS) are able to generate reactive oxygen species (ROS) such as hydroxy radicals and singlet oxygen ($^1O_2$) from oxygen molecules in response to near-infrared (NIR) irradiation; these ROS then critically damage tumor cells [24,25]. However, the therapeutic performance of PDT is inhibited in hypoxic tumor regions because of the dependence of this method on tissue oxygen level and light intensity. Moreover, most PS agents have a maximum absorption of ~660 nm, and light of this wavelength cannot fully penetrate deep tissues compared to NIR light (700–980 nm) [26–28]. Upconverting nanoparticles (UCNPs) capable of emitting shorter wavelength light from longer excitation light based on the anti-Stokes phenomenon have been utilized to increase penetration depth and illumination efficiency. In particular, UCNPs that absorb light at wavelengths of 700–980 nm and emit light of ~660 nm can trigger PS in the body. Lanthanide element-doped core@shell UCNPs consisting of a sensitizer and an activator have been widely used to maximize upconversion activity [29–32].

Hyperthermia is another antitumor therapy. Severe hyperthermia (>48 °C for 10 min) is known to induce rapid apoptosis and irreversible death of tumor cells [33]. By contrast, mild hyperthermia of 39–42 °C enhances the delivery of antitumor therapeutics to the tumor due to increased blood flow and improved vascular permeability of either the drug or nanoparticles due to enlargement of the pores of tumor blood vessels [34–36]. Also, mild hyperthermia helps increase oxygen levels (e.g., partial oxygen pressure (pO_2) and oxy-hemoglobin (HbO_2)) in solid tumors, potentiating the antitumor efficacy of chemotherapeutics [37,38]. Consequently, using hyperthermia in conjunction with primary antitumor modalities can enhance the effectiveness of antitumor therapy. Many conventional photothermal agents, such as indocyanine green, IR780, and gold nanorods, can be used to control the surface temperature in response to NIR laser irradiation depending upon laser intensity, irradiation time, and the concentration of photothermal agents among other factors [39–42].

Herein, we introduce *in situ* injectable versatile erythrocyte-sized microgel platforms (5–6 μm) with controlled photothermal and photodynamic activity that generate heat, O_2, and ROS in response to NIR light. Microgels (Hb μGel) comprised (i) hemoglobin to supply oxygen and emit heat in response to 808 nm laser irradiation, (ii) albumin to stabilize the μGel system, and (iii) UCNPs to emit ~660 nm light in

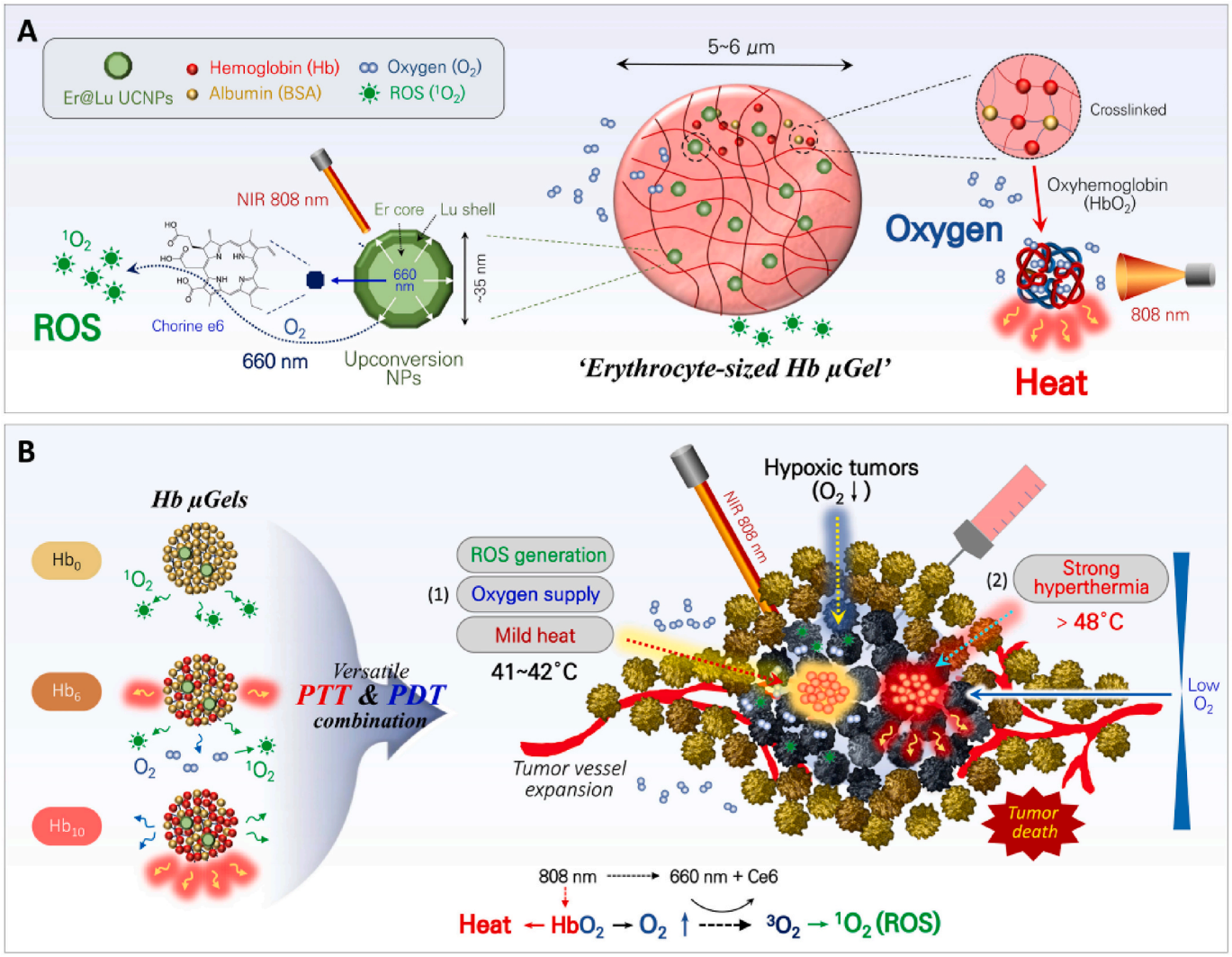

Fig. 1. Schematic illustration showing heat, oxygen, and reactive oxygen species-generating erythrocyte-sized hemoglobin microgels (A) and the use of these microgels for photothermal and photodynamic therapy in hypoxic tumors (B).

response to deep-penetrating 808 nm laser illumination to activate a photosensitizing agent (Ce6) and produce singlet oxygen ($^1O_2$). We hypothesized that these Hb μGels would be able to elevate the O_2 level in hypoxic tumors and potentiate the cytotoxic effect of photodynamic therapy in conjunction with UCNPs. In addition, we posit that heat emission from Hb in response to NIR laser irradiation (808 nm) would help expand the tumor vasculature due to locally elevated temperature (41–42 °C) or could ablate malignant tumors due to severe hyperthermia (>48 °C). Our UCNP/Ce6-loaded Hb μGels are versatile photothermal and photodynamic injectable agents that can overcome the obstacles associated with treatment of hypoxic tumors (Fig. 1).

2. Results and discussion

2.1. Fabrication and characterization of UCNPs

First, we fabricated UCNPs capable of activating a photosensitizer (Ce6) and incorporating into the Hb microgel structure. Our goal was to fabricate UCNPs that efficiently emit 660 nm light upon 808 nm excitation for Ce6 activation. We sought to prepare simple UCNPs consisting of only two components, an erbium (Er) core and a lutetium (Lu) shell, that predominantly emitted red fluorescence emission (~660 nm) in response to 808 nm NIR light. The optimized 660 nm emission of UCNPs is inevitable because the quantum efficiency of regular UCNPs is usually very low (<1%) [43,44]. The highest NIR-to-visible efficiency for UCNPs is 5% even when using deeply penetrating long wavelength light (800–1200 nm) and high irradiation (~100 W/cm$^{2)}$ [45]. Furthermore, UCNPs should be able to disperse well in water to prevent rapid sedimentation or aggregation in response to a high metal density during the emulsification step.

As shown in Fig. 2A, core-only (Er) and core@shell (Er/Lu) UCNPs typically had sharpened edges and were hexagonal in shape. The size of Er core nanoparticles was optimized by varying the Er/F ratio and NH_4F amount (Fig. S1). The final particle sizes of core-only (Er) and core@shell (Er/Lu) UCNPs were ~25 and ~35 nm, respectively (Figs. 2B and S1), indicating that these particles were small enough for colloidal dispersion without critical sedimentation (Fig. 2C). Unlike other conventional lanthanide-based UCNPs (herein, $NaYF_4$: Yb, Nd, Er@$NaLuF_4$ UCNPs), the prepared Er@Lu ($NaErF_4$@$NaLuF_4$) UCNPs presented predominant red emission (>96.7%) around 660 nm but negligible green emission (<3.3%) around ~540 nm, which effectively activated Ce6. Also, our $NaErF_4$@$NaLuF_4$ UCNPs were found to have significantly higher emission intensity (>2.7 fold) around 660 nm, when compared with conventional formula for $NaYF_4$: Yb, Nd, Er@$NaLuF_4$ UCNPs (Fig. S2) in response to 808 nm laser irradiation [29,30].

In our Er@Lu UCNPs ($NaErF_4$@$NaLuF_4$ NPs), Er^{3+} played both roles as sensitizer and activator, absorbing photons and donating the photons to Er^{3+} itself and thereby undergoing multi-step excitation owing to energy transfer [46,47]. This process generates upconverting luminescence. Moreover, the Lu^{3+}-shell plays a role in confining the excited energy within core lattices and strengthening the upconversion emission by preventing surface quenching [29,30,48]. TEM images, element mapping, and EDS spectra for Er@Lu UCNPs shown in Fig. 2D, E and F, respectively, revealed the distribution of Er and Lu in the core and shell of UCNPs. X-ray diffraction (XRD) spectral patterns of the prepared Er@Lu UCNPs ($NaErF_4$@$NaLuF_4$ Core@Shell NPs) were consistent with the representative peaks of previously reported UCNPs [30,49]: all peaks corresponded to (100) (110) (101) (200) (111) (201) (210) (211) (112) (220) and (311) lattice planes of pure hexagonal phase of $NaErF_4$ standard pattern (JCPDS #27–0689). The overall result indicated that our Er@Lu UCNPs were successfully synthesized with the hexagonal phase crystals (Fig. 2G) and strong performance for photodynamic activity [50,51].

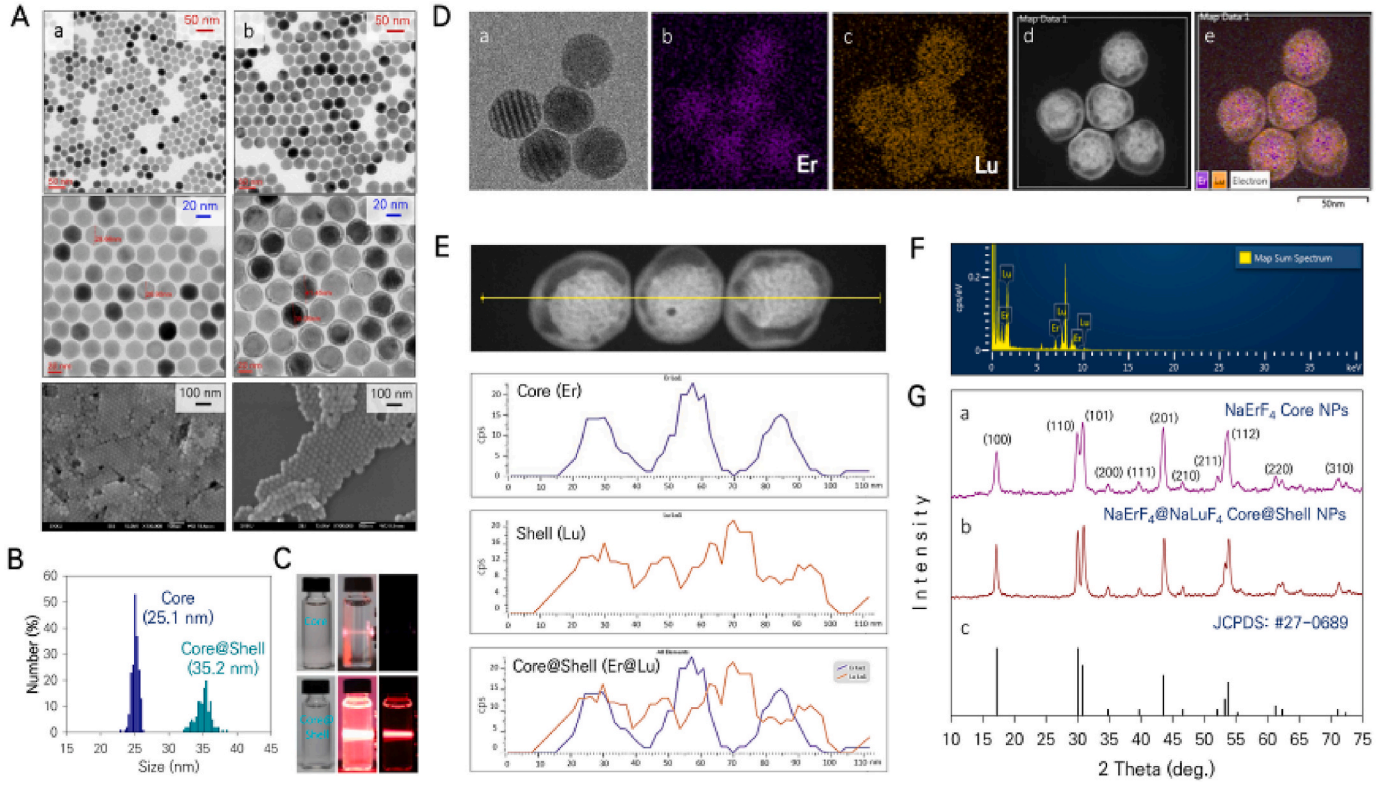

Fig. 2. (A) TEM images of (a) core only and (b) core@shell UNCPs. (B) Histograms of particle sizes of (a) core only and (b) core@shell UNCPs. (C) Photographs of dispersed solutions of Er or Er@Lu UNCPs emitting red fluorescence when irradiated with 808 nm laser. (D) (a) TEM image of Er@Lu UCNPs, (b) and (c) element mapping of core and shell, respectively, (d) electron mapping, (e) merged image. (E) Er and Lu distribution profiles of UCNPs. (F) EDS (electron dispersive spectroscopy) spectrum of Er@Lu UCNPs. (G) XRD spectra of (a) core UNCPs, (b) core@shell UNCPs, (c) JCPDS: 27–0689 ($NaErF_4$).

2.2. Preparation and characterization of hemoglobin microgels

Erythrocytes are the most abundant cells in blood and have multiple biological functions including oxygen delivery [12]. Erythrocytes are viewed as natural transport agents for drug delivery because there is abundant intracellular space for drug loading and their physical structure and size can aid in immune cell evasion [11]. Drug-encapsulated or surface-modified erythrocytes can function as circulating depot systems by protecting the drugs from phagocytosis, resulting in gradual release of drugs into the blood and attenuation of drug-related toxicity [52]. There have been several successful attempts to mimic the biological functions and physical shape/structure of erythrocytes for drug delivery [3,10,11]. Precise micro-size control of oxygen carriers similar to erythrocytes is important because the size of oxygen carriers affects physical contact with relevant cells and cellular uptake by adjoining cells as well as phagocytic cells [53].

We prepared hemoglobin microgels (Hb μGels) similar in size to natural erythrocytes and with a roughly similar shape though without the concave depression characteristic of natural erythrocytes. Hb μGels were facilely prepared using a well-established membrane emulsification method involving the use of Shirasu porous glass (SPG) membranes (Fig. S3). In agreement with the significant accomplishments by Ito et al. [53–55], the size of our Hb μGels could be controlled by adjusting the pore size of the SPG membranes; in particular, extrusion emulsification (w/o) using a hydrophobic SPG membrane with 3-μm pores resulted in the best size matches of our Hb μGels (5–6 μm) with that of erythrocytes (5–7 μm) (Fig. S4). As shown in Fig. 3A, our Hb μGels prepared using different amounts of hemoglobin and albumin (fluorescein-labelled)

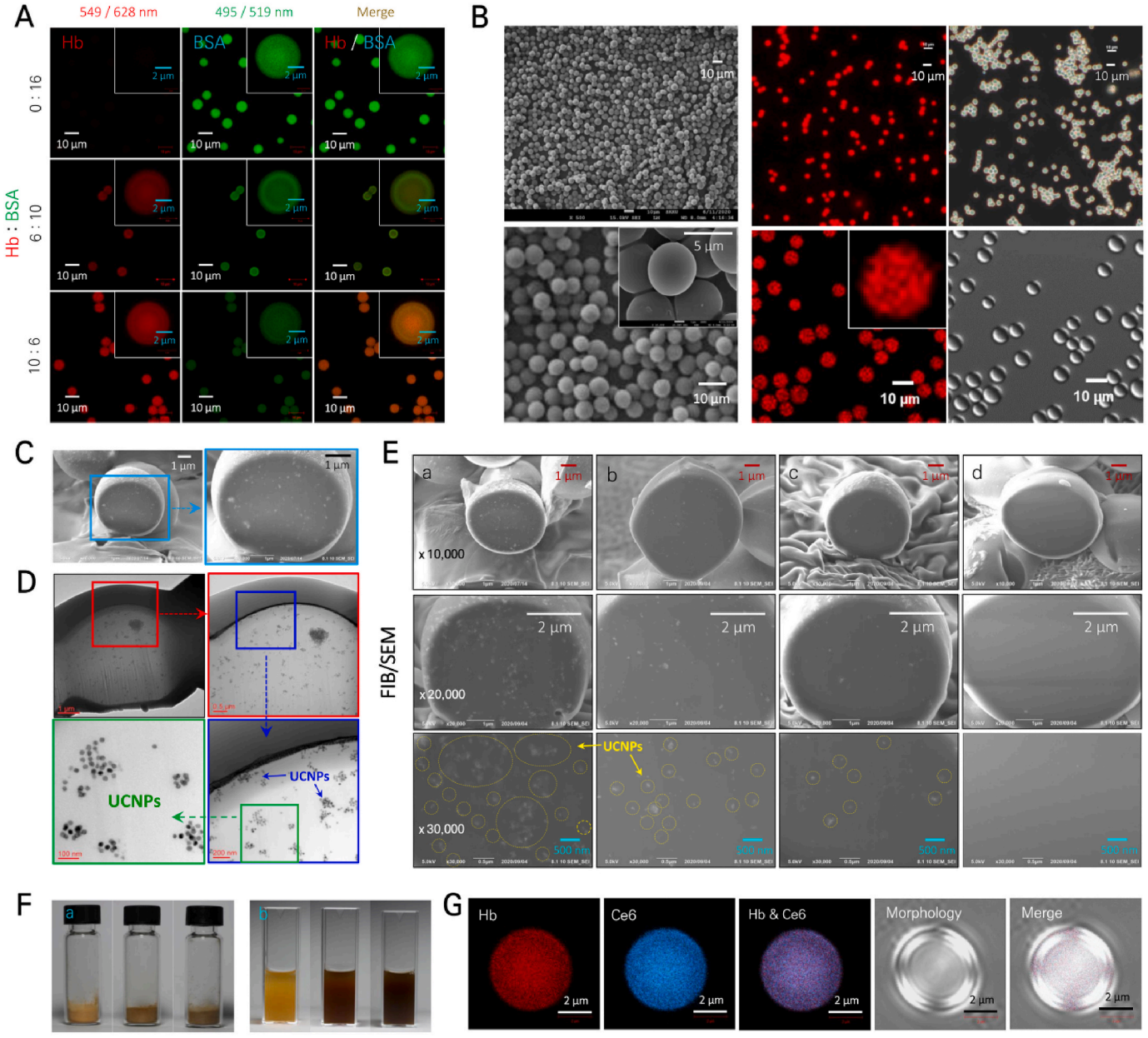

Fig. 3. (A) CLSM images of microgels of Hb and BSA using various weight-based feed ratios (Hb:BSA) of (i) 0:16, (ii) 6:10, and (iii) 10:6 (Hb and BSA-FITC fluorescence measured using Ex/Em wavelengths of 549/628 nm and 495/519 nm, respectively). (B) SEM (left), fluorescence microscopy (right top), and CLSM (right bottom) images of Hb_6 μGels. (C) Focused ion beam (FIB)-based SEM images of Er@Lu UCNP-loaded Hb_6 μGel. (D) FIB-TEM images of Er@Lu UCNP-loaded Hb_6 μGel. (E) FIB-SEM images of Er@Lu UCNP-loaded Hb_6 μGels prepared using different UCNP amounts (a: 120 mg, b: 60 mg, c: 30 mg, d: 0 mg). (F) Photographs of (a) dry powder and (b) dispersed solutions of Hb_0 μGel, Hb_6 μGel and Hb_{10} μGel. (G) CLSM images of Hb_6 microgels with Er@Lu UCNPs and Ce6.

were visualized by confocal laser scanning microscopy (CLSM). Red or green fluorescence indicated the presence of Hb and BSA, respectively. A greater Hb feed amount led to greater red fluorescence intensity, indicating higher incorporation of Hb into the respective Hb μGels. Hb_6 μGels were homogenously spherical and highly uniform in size (~6 μm) (Fig. 3B). Our next important goal was to incorporate large quantities of Er@Lu UCNPs into the Hb μGel during membrane emulsification and gelation. Er and Lu are very heavy (density: 9.2 and 9.7 g•cm^{-3}, respectively), and the surfaces of oleate-capped Er@Lu UCNPs are hydrophobic and minimally water-dispersible. Sedimentation and aggregation of Er@Lu UCNPs should be prevented by substitution with the hydrophilic polyacrylic acid (PAA) [56]. The resulting PAA-coated Er@Lu UCNPs were well dispersed in water and phosphate buffer over 12 h without significant precipitation or particle agglomeration, when compared with oleate (OA)-coated Er@Lu UCNPs. This enhanced dispersibility probably ensured their stable incorporation into the water phase during membrane emulsification (<60 min) (Fig. S5), showing the relatively high encapsulation efficiency of >63%.

Incorporation of UCNPs into Hb μGels was identified by focused ion beam (FIB)-scanning electron microscopy (SEM) and transmission electron microscopy (TEM); the water phase-dispersed UCNPs were stably embedded throughout the internal network structure of Hb μGels based on cross-sectional surface analysis (Fig. 3C), and the presence of incorporated UCNPs was also confirmed using TEM (Fig. 3D). As shown in Fig. 3E, the amount of incorporated UCNPs was proportional to the respective feed amount (0–120 mg). As-prepared Er@Lu UCNP-loaded Hb μGels prepared at different feed amount ratios of Hb and BSA (0:16, 6:10, and 10:6) had distinctive powder colors and were well dispersed in solution as fine micro-suspensions without aggregation (Fig. 3F). The photosensitizer Ce6 was directly incorporated into the Hb_6 μGels (+UCNPs) at the final step for photodynamic activity, and the Ce6-containing Hb_6 μGels were visualized using CLSM at wavelengths appropriate for Hb and Ce6, respectively (Fig. 3G). In general, surface Ce6-conjugated UCNPs (i.e., UCNPs@SiO_2) have been utilized in intravenous route for photodynamic therapy in terms of high energy transfer. However, a direct loading method for Ce6 was considered more efficient for local delivery because additional Ce6 conjugation step onto UCNPs was associated with practical inefficiency at our microgel system, such as, restricted conjugation yield and reduced dispersability of UCNPs owing to low Ce6 solubility.

2.3. Photothermal activity of Hb μGels

We next examined the pharmaceutical performance of the various Hb μGels including Er@Lu UCNP/Ce6-loaded Hb μGels in terms of the generation of heat, oxygen and singlet oxygen (ROS). First, the photothermal ability of Hb μGels was evaluated. As with porphyrins with pyrrole rings and unsaturated linkers, heme (iron protoporphyrin IX), a major component of Hb, efficiently absorbs visible bandwidth light much more than other blood components [57]. In particular, heme derivatives coordinated with metal ions effectively absorb light and have strong photothermal as well as photodynamic effects [57,58]. For example, porphysome nanovesicles were shown to display strong hyperthermia comparable to that of gold nanorods in response to 673 nm laser irradiation [58]. Previously, we reported concentration-dependent hyperthermal activity in *in situ* PEGylated hemoglobin hydrogels; these hydrogels had surface temperatures of ~70 °C at 100 mg/ml feed concentration under 808 nm irradiation [59]. This was due to considerable absorption of NIR red light (700–900 nm) by hemoglobin. Similar to our previous findings [59], the Hb μGels showed hyperthermal activity under 808 nm laser irradiation that was comparable to that of naïve Hb (Fig. S6).

As shown in Figs. 4A, B and S7, Hb_{10} or Hb_6 μGels (30 mg/mL) had surface temperatures up to ~58 and 46 °C, respectively, after 15 min under 808 nm-laser irradiation (1.5 W/cm^2), whereas Hb_0 μGels (BSA μGel without any Hb) emitted little heat under the same conditions. The photothermal activity of Hb μGels according to Hb feed amount was also visualized by photothermal camera (Fig. 4C). Hb μGels showed photothermal activity only when irradiated with 808 nm laser light. Local hyperthermia around 41–42 °C could be precisely tuned by controlling irradiation time and intensity (Fig. 4D). Mild hyperthermia (42–48 °C) of mice tumors was achieved using Hb μGels (Hb:BSA = 10:6 or 6:10) and 808 nm laser irradiation, whereas the surface temperature of mice tumors treated with PBS or Hb_0 μGel did not increase appreciably (Figs. 4E, F and S8).

2.4. Oxygen-carrying and photodynamic activity of Hb μGels

Circular dichroism spectra of Hb μGels showed little similarity with those of its major component materials (Hb and BSA) in the wavelength range of 190–260 nm. Wavelengths of each Hb μGel formula (Hb:BSA = 10:6, 6:10 or 0:16, respectively) appeared to be around 228–234 nm, whereas Hb and BSA had 222 or 210 nm troughs because of the large size of Hb μGels (>5 μm) (Fig. 5A). The major hemoglobin form used in this study was acellular methemoglobin (Fe^{3+}), which has a low oxygen-binding/carrying affinity [5]. Therefore, met-Hb should be reduced to ferrous Hb (Fe^{2+}), which is more likely to bind to oxygen as an oxyhemoglobin; ascorbic acid can then be used to reduce met-Hb to ferrous Hb for further facile conversion to (de)oxy-Hb.

Representative UV-VIS spectra peaks for met-Hb and oxy-Hb were observed at ~406 and ~412 nm, respectively [60,61]. Similarly, our Hb_6 μGel and ascorbic acid-reduced Hb_6 μGel (presumably oxygenated Hb μGel) had UV-VIS spectral peaks at ~408 and ~413 nm, respectively (Fig. 5B). However, our Hb_6 μGel did not display two distinct peaks at ~540 and ~575 nm, which are representative of oxy-Hb (data not shown). The colors of both Hb and Hb_6 μGel solutions became browner upon addition of ascorbic acid (final concentration of 6 mM) (Fig. 5C). As shown in Fig. 5D, the nitrogen-purged hypoxic Hb_6 μGel sample contained very little oxygen, whereas oxygenated Hb_6 μGel showed immediate increase in the O_2 concentration in a hypoxic solution. Furthermore, oxygenated Hb_6 μGel with ascorbic acid (6 mM) increased the O_2 concentration significantly (vs. Hb_6 μGel without ascorbic acid), and this O_2 concentration was maintained for 20 min. The increase of O_2 concentration by Hb_6 μGel (+ ascorbic acid & oxygen) was higher than that of Hb_0 μGel (+ PFC & oxygen). However, Hb_0 μGel (+ PFC & oxygen), which included a PFC-loaded BSA nanoemulsion (PFC/BSA-NE; Fig. S9), exhibited a second episode of oxygen release when treated with ultrasound for 5 min. These results indicated that oxygenated Hb_6 μGels (if additionally formulated with PFC/BSA-NE) can deliver a prolonged oxygenation effect under hypoxic conditions. Finally, the singlet oxygen ($^1O_2$)-generating ability of each Hb μGel was evaluated under normoxic, hypoxic, or oxygenated conditions.

As mentioned above, $^1O_2$-generation efficiency is critically determined by oxygen level, from which singlet oxygen are generated. Thus, photodynamic antitumor therapy using photosensitizers is not effective in severely hypoxic cancers. Nitrogen-purged hypoxic UCNP/Ce6-loaded Hb_6 μGel samples generated no significant $^1O_2$, whereas oxygenated UCNP/Ce6-loaded Hb_6 μGels induced $^1O_2$ production even under hypoxic conditions. Importantly, UCNP/Ce6-loaded Hb_6 μGels (+ ascorbic acid & oxygen) resulted in gradual generation of $^1O_2$ over 60 min, and the $^1O_2$-generating ability of these gels was higher than that of UCNP/Ce6-loaded Hb_0 μGels (+ PFC & oxygen) (Fig. 5E). Singlet oxygen sensor green (SOSG) oxidized by singlet oxygen ($^1O_2$) forms SOSG endoperoxide (SOSG-EP), providing strong fluorescence signals. The SOSG signal intensity from microplate wells for corresponding samples were visualized at predetermined times using a fluorescence imaging system (NeoScience, Suwon, Korea). As shown in Fig. 5F, the SOSG signal intensity of the groups with supplied oxygen gradually increased with the color change from green to red. Especially, UCNP/Ce6-loaded Hb_6 μGels (+ ascorbic acid & O_2) displayed the strongest red fluorescence signal at 60 min, when compared with other groups.

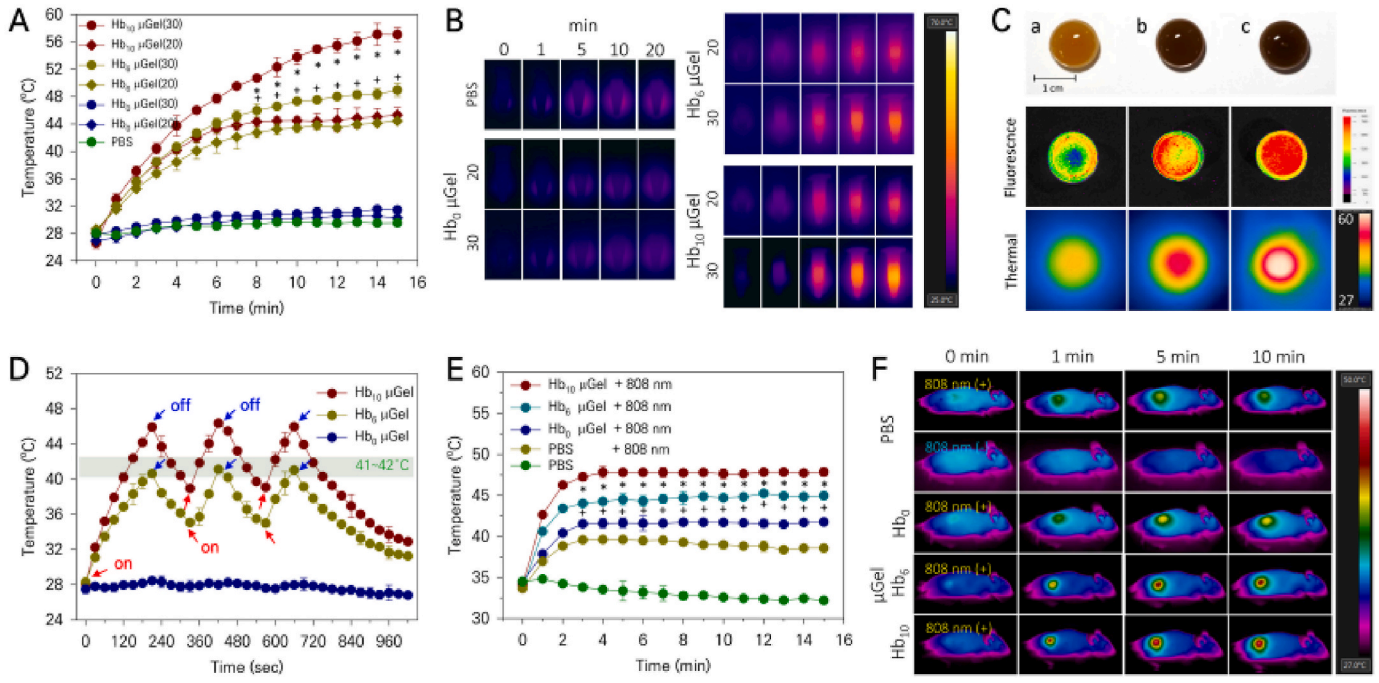

Fig. 4. (A) Kinetic changes in surface temperatures of Hb μGels (20 or 30 mg/ml each) under NIR laser irradiation (808 nm, 1.5 W/cm^2). ^{+}P and $^{*}P < 0.006$ over Hb_{10} μGel (20) and Hb_6 μGel (20), respectively. (B) Thermographic images of PBS and Hb μGels under NIR laser irradiation (808 nm, 1.5 W/cm^2). (C) Fluorescence and thermographic images of Hb_0, Hb_6, and Hb_{10} μGels irradiated by laser (808 nm, 1.5 W/cm^2). (D) Mild hyperthermia (41–42 °C) induced by Hb_0, Hb_6 and Hb_{10} μGels with alternation of on/off 808 nm light irradiation. ^{+}P and $^{*}P < 0.005$ over Hb_0 μGel +808 nm and Hb_6 μGel +808 nm, respectively. (E) Tumor temperature change profiles of Hb μGel groups with or without 808 nm laser irradiation (0.3–0.5 W/cm^2) in a mild hyperthermia setting (41–42 °C). (F) *In vivo* whole-body thermal images of 4 T1 tumor-bearing mice treated with PBS, Hb_0, Hb_6 or Hb_{10} μGels.

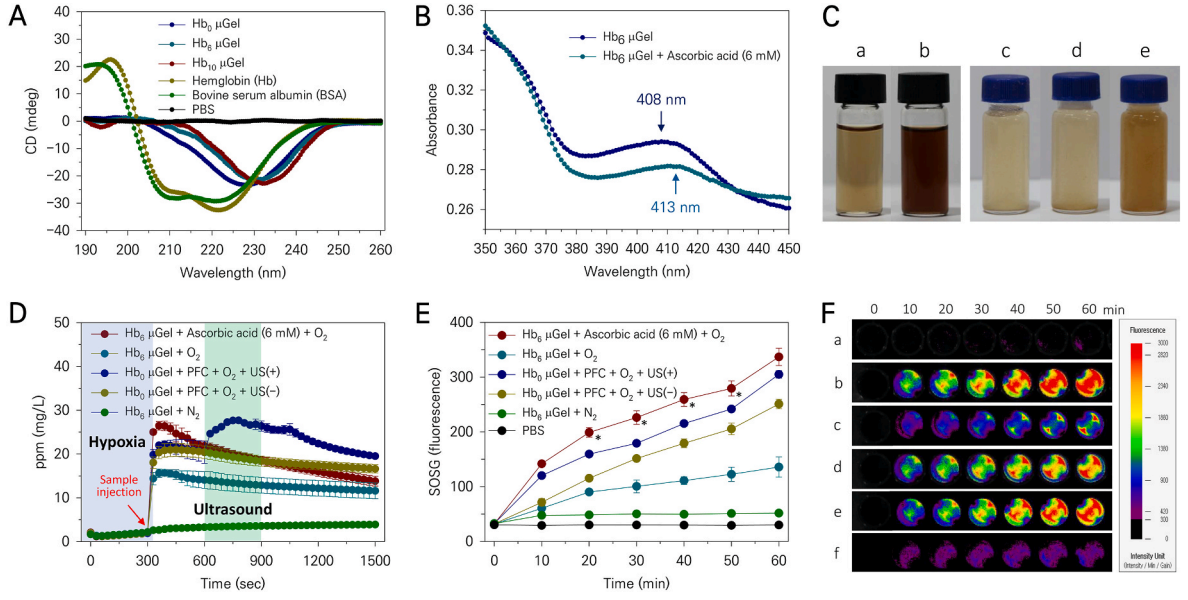

Fig. 5. (A) Circular dichroism spectra of PBS, naive Hb, BSA or Hb_0, Hb_6, and Hb_{10} μGels. (B) UV-VIS spectra of naive or ascorbic acid-treated Hb_6 μGels. (B) Singlet oxygen generation profiles of PBS and the various Hb μGel groups under different conditions. (C) Photographs of naive Hb (a) and Hb_6 μGel (c) or ascorbic acid-treated-Hb (b) and ascorbic acid-treated-Hb_6 μGel (d), and ascorbic acid-treated/oxygenated-Hb_6 μGel (e). (D) Oxygen generation profiles of the various Hb_6 μGel groups under different conditions. (E) SOSG fluorescence profiles showing the amount of singlet oxygen produced at each time point (Ex/Em = 485/538 nm). $^{*}P < 0.01$ over Hb_0 μGel + PFC + O_2 + US(+). (F) Fluorescence images of each microplate well showing the production level of singlet oxygen at various time points: (a) PBS; (b) Hb_6 μGel + ascorbic acid (6 mM) + O_2; (c) Hb_6 μGel + O_2; (d) Hb_0 μGel + PFC + O_2 + US(−); (e) Hb_0 μGel + PFC + O_2 + US(+); (f) Hb_6 μGel + N_2.

2.5. *In vitro cytotoxic evaluation of Hb μGels in hypoxic cell spheroids*

We next evaluated the cytotoxicity of our UCNP/Ce6-loaded Hb μGels (Hb_{10} or Hb_6 μGel) to hypoxic 4T1 cell spheroids. Given the relatively large size (~6 μm) of our Hb μGels compared to 4T1 cells, we did not use 2D cell beds for cytotoxicity evaluation because these cell beds became tightly attached and covered with a large quantity of Hb μGel even at a relatively low concentration (0.5–2.0 mg/ml) vs. the concentration used in the spheroid system (>20 mg/ml), which presumably resulted in temporary unwanted hypoxia, abnormal physiology

and eventually cell death (Fig. S10). Hence, three dimensional 4T1 spheroids (~500 μm) were chosen for the staining-based *in vitro* cytotoxicity evaluations, such as, Live/Dead™, ROS production and HIF-1α assay. As shown in Fig. 6A, UCNP/Ce6-loaded Hb μGels were well dispersed in media and contacted the outer layer of 4T1 spheroids. Hb μGels are unlikely to penetrate cells or the deep inner space of spheroids given their large size (5–6 μm vs. each cell 30–40 μm) (Fig. S11). Hypoxia was achieved in a hypoxic chamber using a hypoxic gas stream (5% CO_2/95% N_2) and confirmed by visualizing hypoxia-inducible factor (HIF)-1α expression.

As shown in Fig. 6B, spheroids subjected to hypoxic conditions stained strongly with anti–HIF–1α antibody (emitted bright green fluorescence). By contrast, normoxic spheroids did not stain with anti–HIF–1α antibody [23]. Significantly, 4T1 spheroids treated with either UCNP/Ce6-loaded Hb_6 μGels (+ ascorbic acid & oxygen) or UCNP/Ce6-loaded Hb_0 μGels (+ PFC & oxygen + US scan) did not produce a hypoxic fluorescence signal. Intracellular $^1O_2$ generation in 4T1 cell spheroids was visualized by CLSM. Under hypoxic conditions, all 4T1 cell spheroids incubated with UCNP/Ce6-loaded Hb μGels displayed negligible fluorescence signals, indicating the absence of intracellular $^1O_2$ based on CellROX® Deep Red dye detection regardless of 808-nm laser irradiation (Fig. S12). By contrast, when irradiated with 808 nm laser light, all 4T1 cell spheroids incubated under normoxic or oxygenated conditions with UCNP/Ce6-loaded Hb_6 μGel (+ ascorbic acid & oxygen) or UCNP/Ce6-loaded Hb_0 μGel (+ PFC & oxygen + US scan) emitted strong fluorescence signals. This indicated that our UCNP/Ce6-loaded Hb_6 μGels were able to release or generate both O_2 and $^1O_2$ under hypoxic conditions and thereby kill spheroids (Fig. 6C). The UCNP/Ce6-loaded Hb_6 μGels (+ ascorbic acid & oxygen + 808 nm laser) effectively killed spheroids, whereas naïve UCNP/Ce6-loaded Hb_6 μGels were unable to kill spheroids under hypoxic conditions despite 808 nm laser irradiation. The cytotoxicity of UCNP/Ce6-loaded Hb_6 μGels (+ ascorbic acid & oxygen + 808 nm laser) was comparable to that of UCNP/Ce6-loaded Hb_0 μGels (+ PFC & oxygen + US scan + 808 nm laser) (Fig. 6D).

As shown in Fig. 6E, UCNP/Ce6-loaded Hb_0 μGels displayed a significant photodynamic activity-based cytotoxic effect at a low concentration (20 mg/mL; 808 nm laser 30 min) and under normoxic conditions, while Hb_6 μGels (30 mg/mL without Ce6/UCNPs) showed notable photothermal activity-based cytotoxicity in response to 808 nm laser irradiation (1.5 W/cm^2) for 30 min. As shown in Fig. 6F, UCNP/Ce6-loaded Hb_6 μGels had significant cytotoxic activity with mild hyperthermia (41–42 °C) in conjunction with photodynamic activity under normoxia, whereas Hb_6 μGels were unable to kill 4T1 spheroids despite mild hyperthermia. The strong photothermal activity induced by 808 nm laser irradiation (1.5 W/cm^2 for 30 min) of Hb_6 μGels (~40 mg/mL) effectively killed spheroids, as indicated by the absence of green fluorescence. Additionally, the 808 nm laser irradiation (1.5 W/cm^2 for 60

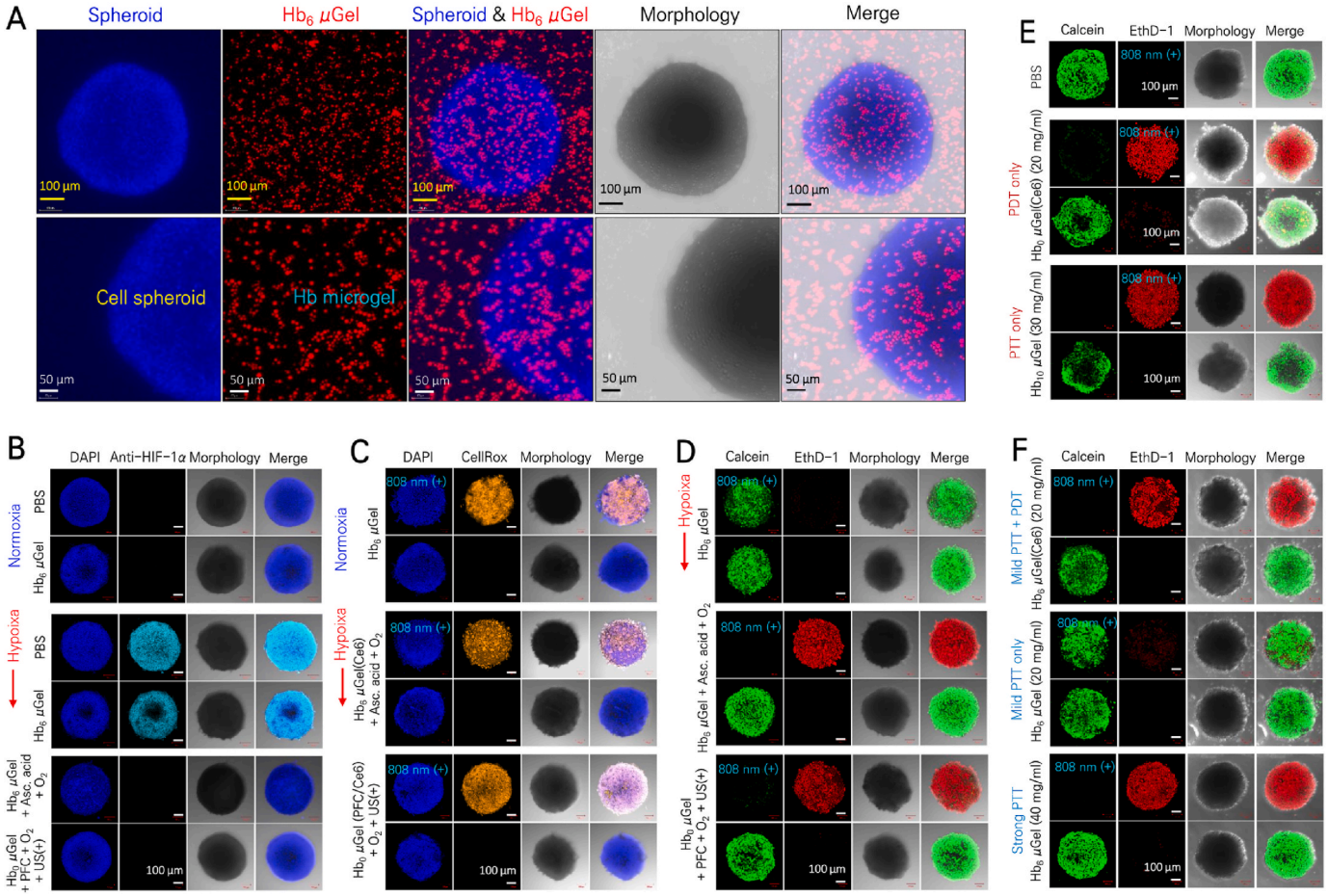

Fig. 6. (A) CLSM images of a 4T1 cell spheroid with dispersed Hb_6 μGel. (B) CLSM images of HIF-1α staining in 4T1 cell spheroids treated with PBS or various Hb μGels under normoxic, oxygenated or hypoxic conditions. (C) CLSM images of intracellular ROS production in 4T1 cell spheroids treated with Hb μGels (+UCNPs/Ce6) with or without 808 nm laser irradiation under normoxic or hypoxic conditions. (D) CLSM images of live/dead 4T1 cell spheroids incubated with Hb μGels (+UCNPs/Ce6) with or without 808 nm laser irradiation under hypoxic or oxygenated conditions. (E) CLSM images of live/dead 4T1 cell spheroids incubated with PBS, Hb_6 μGel (+UCNPs/Ce6) or Hb_{10} μGel with or without 808 nm laser irradiation under normoxic conditions. (F) CLSM images of live/dead 4T1 cell spheroids incubated with PBS or Hb_6 μGel (+UCNPs/Ce6) with or without 808 nm laser irradiation specifically adjusted to induce mild (41–42 °C) or high (>48 °C) surface temperatures. Green and red represent live and dead cells, respectively.

min) alone hardly exhibited significant temperature increase and deleterious effect on the 4T1 spheroid viability (Figs. 6D, E and S12). Therefore, the overall cytotoxicity to 4T1 tumor cells was obviously due to the combined effects by photothermal and photodynamic activity aided by O_2 supply.

2.6. *In vivo imaging and tumor oxygenation of Hb μGels in hypoxic mice tumors*

The presence of metal (Er/Lu) components was clearly detected in UCNP/Ce6-loaded Hb_6 μGels by computed tomography (CT). Especially, Lu shell-based UCNPs possess prominent spectral X-ray CT performance, which is considered even better than that of clinical used Iohexol® and provides improved diagnostic interpretation [62]. As shown in Fig. 7A, UCNP/Ce6-loaded Hb_6 μGels were detected at the injection site of mouse tumors up to 1 day after injection. However, a negligible quantity of UCNP/Ce6-loaded Hb_6 μGel was present at the tumor site on day 7. After intratumor injection of UCNP/Ce6-loaded Hb_6 μGels (including Hb and Cy5.5-BSA) in 4T1 tumor-bearing mice, Hb and Cy5.5 fluorescence were visualized. Considerable amounts of fluorescence from both Hb and Cy5.5 were present for up to 12 h, but the NIR-fluorescence signals decreased gradually and then faded at 168 h after intratumor injection (Figs. 7B and S13). Accumulation of oxygen (as HbO_2) in the 4T1 tumors of mice was visualized by photoacoustic (PA) analyses with high resolution and deep imaging depth (Fig. 7C). Intratumor injection of PBS and hypoxic Hb_6 μGel (purged with N_2) generated very little oxygen (20–30% over 60 min). However, intratumor injection of Hb_6 μGel (+ ascorbic acid & oxygen) effectively elevated the tumor oxygen level (>60%) at 0–30 min, comparable to that achieved by Hb_0 μGel (+ PFC + US(+)) (>55–65% over 30 min) (Fig. 7D). These findings demonstrated that our Hb_6 μGel were able to supply oxygen to ameliorate hypoxia in solid tumors.

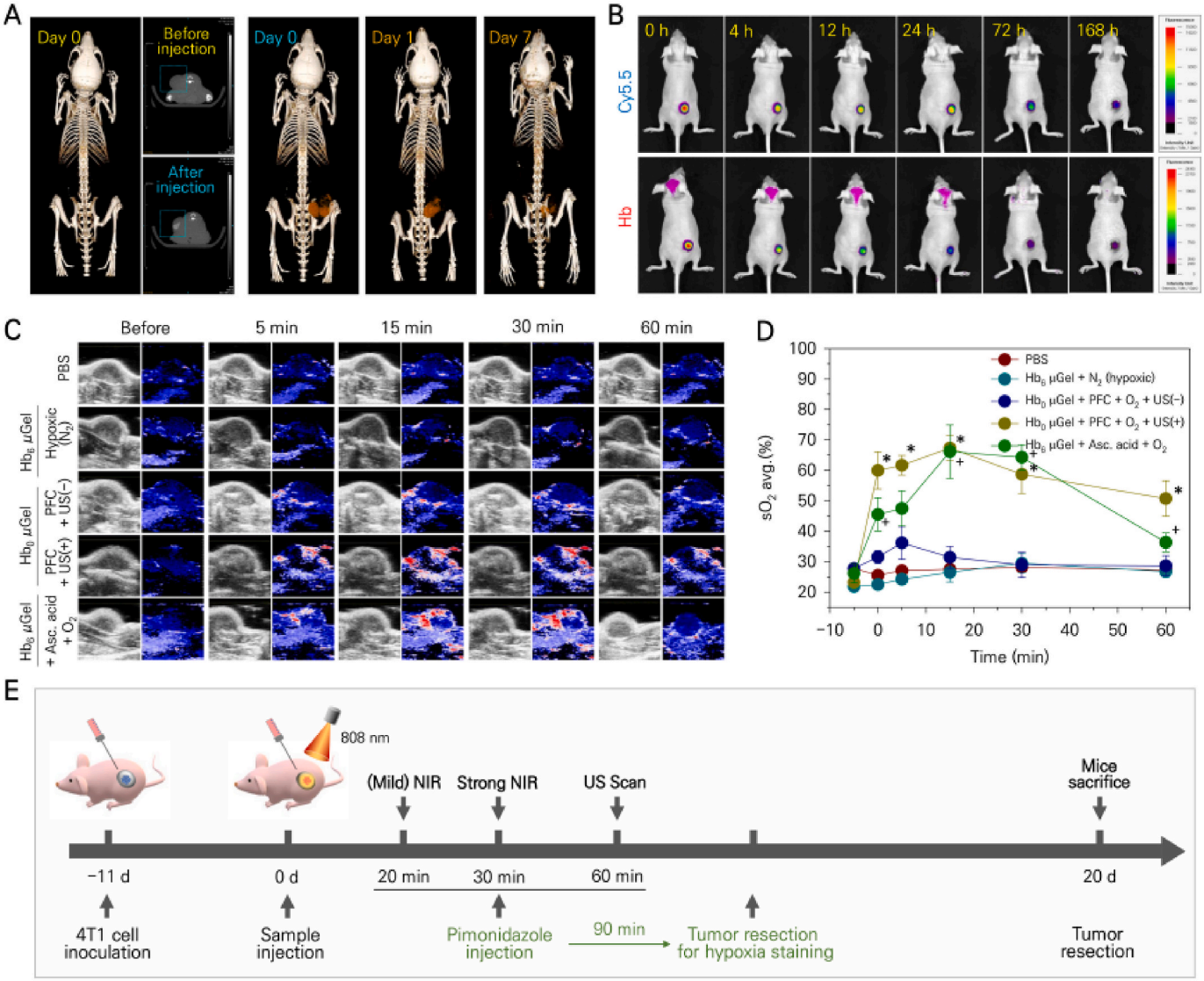

Fig. 7. (A) Computerized tomography (CT) images of 4T1 tumor-bearing mice intratumorally injected with UCNP-loaded Hb_6 μGels. (B) *In vivo* visualization of 4T1 tumor-bearing mouse after intratumor injection of Hb_6 μGel based on Cy5.5 and Hb fluorescence at 630 and 730 nm, respectively. (C) Photoacoustic images showing 4T1 tumor oxygenation before and after intratumor injection of PBS or various Hb_6 μGels (+ ascorbic acid or PFC) with or without ultrasound (US) treatment. (D) Oxygen level profile of 4T1 tumors before and after intratumoral injection of PBS or various Hb_6 μGels (+ ascorbic acid or PFC) under different conditions. $^{+}P < 0.003$, $^{*}P < 0.001$ and $^{*}P < 0.05$ over the group of Hb_0 μGel + PFC + O_2 + US(−). (E) Brief schedule for *in vivo* antitumor efficacy experiment using a 4T1 xenograft mice model.

2.7. *In vivo antitumor efficacy of intratumor-injected Hb μGels in hypoxic mice tumors*

Our final aim was to evaluate the antitumor effect of UCNP/Ce6-loaded Hb μGels in a hypoxic 4T1 tumor-bearing mouse model (Fig. 7E). Mice having tumors of 120–150 mm^3 were randomly divided into seven groups (G1-G7). Hb μGel samples for each group were designated to reveal the differences in antitumor efficacy in terms of hemoglobin content, photodynamic activity, oxygen supplying effect and hyperthermal degree (NIR laser irradiation time etc.). The detailed sample descriptions were presented in Fig. S14. The NIR irradiations for the mild and strong temperature setting and ultrasound scan were performed for 20, 30 and 60 min, respectively. Tumor volumes were measured for 20 days after treatment (Fig. 8A and B). Tumor volumes on day 20 for groups G1 - G7 were 1089.9 ± 79.2, 986.7 ± 22.8, 916.5 ± 104.7, 893.1 ± 22.7, 484.7 ± 23.8, 106.8 ± 83.5, and 49.8 ± 37.2 mm^3, respectively. Compared with G5 mice, there was less opportunity for release and supply of oxygen (from PFC) in mice in G6 due to the

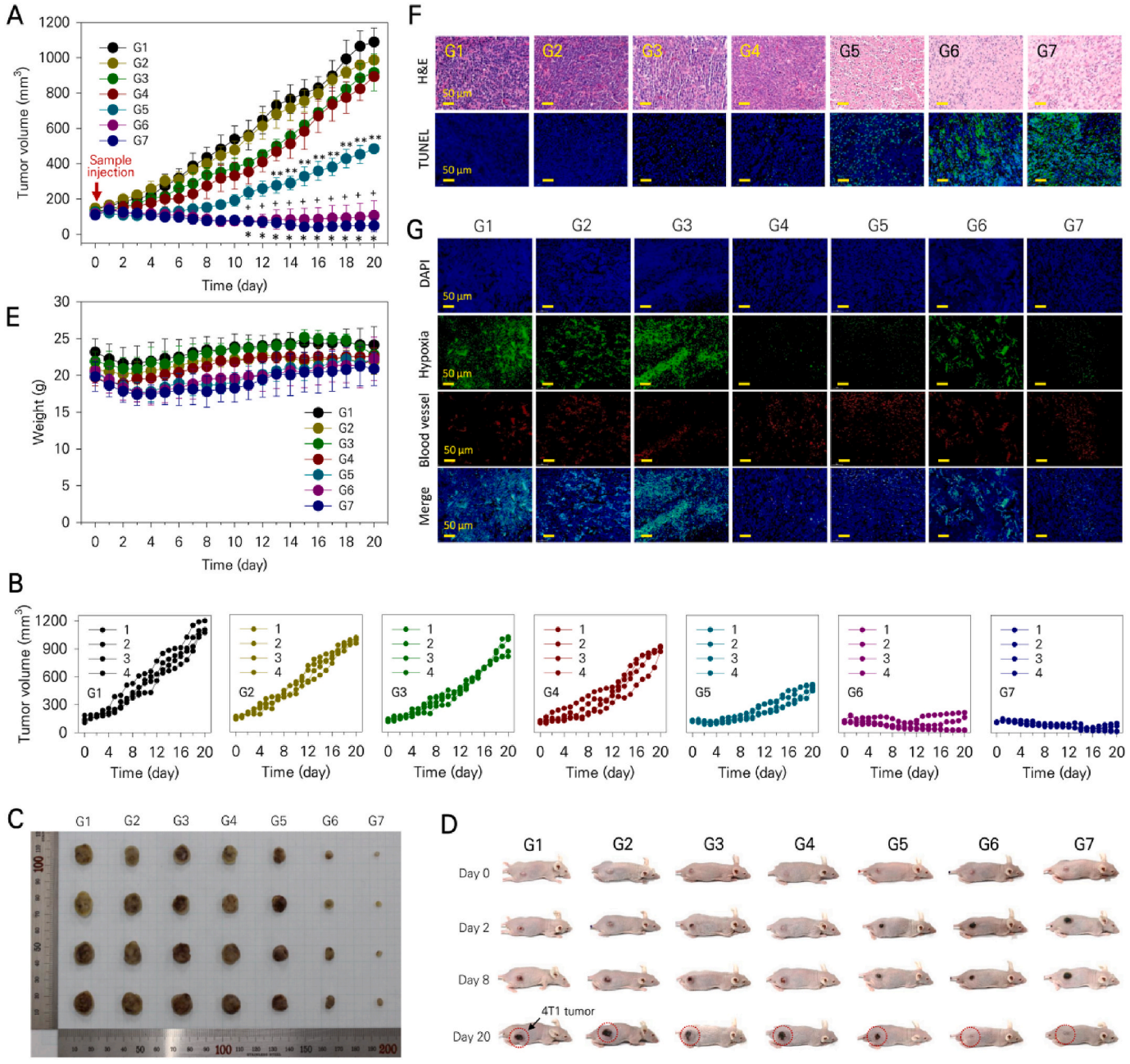

Fig. 8. (A) Profile of tumor volumes of 4T1 tumor-bearing mice treated with G1 - PBS (non-treated); G2 - Hb_6 μGel + 808 nm (+) under a mild temperature (41–42 °C) setting; G3 - Hb_0 μGel (+UCNPs/Ce6) previously treated with nitrogen to maintain a hypoxic state + 808 nm (+) (1.5 W/cm^2 for 20 min); G4 - Hb_6 μGel (+UCNPs/Ce6) + ascorbic acid + O_2 + 808 nm (−); G5 - Hb_0 microgel (+UCNPs/Ce6) + PFC + O_2 + 808 nm (+) + US(+) (60 min); G6 - Hb_{10} μGel (+UCNPs) + 808 nm (+) (1.5 W/cm^2 for 30 min) under strong hyperthermia (>48 °C) and G7 - Hb_6 μGel (+UCNPs/Ce6) + ascorbic acid + O_2 + 808 nm (+) under a mild temperature (41–42 °C) setting.. $^{+}P < 0.003$, $^{*}P < 0.001$ over G5 and $^{**}P < 0.01$ over G4. (B) Individual tumor volume profiles of each mouse group (G1-G7). (C) Photographs of tumors excised from each treatment group. (D) Representative photographs of 4T1-tumor-bearing mice at the indicated days after treatment. (F) Microscopic photographs showing H&E and TUNEL staining of tumor slices from mice in each treatment group. (G) Immunofluorescence imaging of tumor slices from mice treated with each sample. Cell nuclei, blood vessels, and hypoxic regions were stained with DAPI (blue), anti-CD31 antibody (red), and antipimonidazole (green), respectively.

absence of ultrasound treatment. Tumors in G6 or G7 groups were the most noticeably suppressed after treatment with UCNP/Ce6-loaded Hb μGels designed to achieve strong hyperthermia (>48 °C) or photodynamic performance under a mild temperature (41–42 °C) in addition to increasing oxygen levels (Figs. 8C, D and S15). Despite only single treatment during entire *in vivo* experiment, tumors in G6 or G7 groups did not significantly regrow at the primary tumor xenograft site until day 20. Remarkably, tumors of G7* mice (extra n = 3; treated same with G7 but cared until day 30) almost disappeared on day 30 without significant regrowth/recurrence since day 20 (Fig. S15). Body weights of mice in the seven treatment groups were maintained without significant change over 20 days, indicating that all mice were well cared for without deleterious effects for the duration of therapy (Fig. 8E). Separately, we demonstrated that the 808 nm laser irradiation alone (1.5 W/cm^2 for 60 min: no sample injection) seldom elevated the surface tumor temperature and did not suppress the growth of xenograft 4T1 tumors [group H1 (n = 4); tumor volume: 1176.0 ± 76.3 mm^3] (Fig. S15). Also, the tumor suppression profile of another group H2 (n = 4) for Hb_{10} μGel (+UCNPs without Ce6) with 808 nm laser irradiation at mild temperature (41–42 °C) was examined to compare with that of G6 (strong hyperthermia). This new group did not exhibit significant hyperthermal and photodynamic effects due to mild temperature setting and absence of Ce6. The antitumor efficacy of group H2 was much lower than that of G6 but similar with those of G2 or G1 (control PBS) (tumor volume: 962.6 ± 68.0 mm^3; Fig. S15).

Tumors obtained from each treatment group were evaluated histologically by hematoxylin and eosin (H&E) staining and terminal deoxynucleotidyl transferase-mediated dUTP-biotin nick end labeling (TUNEL) (Fig. 8F). H&E-stained tumor tissue specimens from G6 and G7 mice exhibited noticeably lower tumor cell density than specimens from the other mouse groups. The strongest TUNEL fluorescence staining was found in 4T1 tumors from groups G6 and G7 treated with strong hyperthermia or continuous $^1O_2$ exposure, indicating significant tumor cell apoptosis in these groups. Cytotoxicity was achieved by ROS-mediated apoptosis as well as strong and sudden heat stress. Enhanced tumor oxygenation by Hb_6 μGels (+ ascorbic acid & oxygen) and Hb_0 μGels (+ PFC + US(+)) was confirmed using the Hydroxyprobe™-1 (pimonidazole HCl) immunofluorescence staining assay for tissue hypoxia. Pimonidazole (2-nitroimidazole), which is specifically reduced and binds to intracellular macromolecules in hypoxic regions of tumors [63,64], was intraperitoneally injected immediately after the sample injections. Tumors were resected at 90 min after the pimonidazole injection. As shown in Fig. 8G, only 4T1 tumors from G4, G5, and G7 mice were not hypoxic, whereas tumors from mice in the PBS group and other groups showed clear green fluorescence, indicating hypoxia. Together, these results indicate that Hb_6 μGels can supply oxygen to hypoxic tumor tissues, which can help suppress hypoxic tumor growth. Furthermore, the intratumoral injection of Cy5.5-tagged or naïve Hb_6 μGel (+UCNPs/Ce6) resulted in not only negligible accumulation in five major tissue organs (liver, kidney, spleen, lung and heart) but insignificant changes in tissue histology based on H&E staining. This showed that our hemoglobin μGels were presumably biocompatible and safe as a promising injectable microgel system because it mainly consisted of generally-regarded biocompatible hemoglobin and albumin proteins (Figs. 8E and S16).

3. Conclusions

In summary, we successfully designed and prepared erythrocyte-like Hb μGel systems of 5–6 μm in size comprising Er@Lu UCNPs and Ce6 photosensitizer and capable of (i) emitting heat, (ii) supplying oxygen, and (iii) generating singlet oxygen in response to 808 nm NIR laser irradiation. Our Hb μGels were able to elevate the surrounding temperature by emitting heat in a controlled manner (either strong or mild) and also to generate singlet oxygen under sufficient self-oxygenation due to the activity of UCNPs and the affinity of heme for oxygen. By varying synthesis conditions, Hb μGels can be designed to have either photothermal or photodynamic activity or both to effectively suppress hypoxic tumor spheroids and mice tumors. Mild hyperthermia induced by Hb μGels plays a supporting role in killing hypoxic tumor cells because it facilitates the local transport of O_2 and $^1O_2$. Importantly, all these abilities can be achieved using a single Hb μGel system in combination with NIR laser irradiation. Taken together, our results validate Hb μGels as prototype locally injectable microgel platforms for the treatment of hypoxic tumors.

4. Materials and methods

4.1. Materials

Erbium acetate hydrate (III), lutetium acetate hydrate (III), ammonium fluoride (NH_4F), oleic acid, 1-octadecene, ammonium hydroxide solution, polyacrylic acid (Mw 1,800), hemoglobin (Hb; bovine), bovine serum albumin (BSA), and kerosene were purchased from Sigma-Aldrich (St. Louis, MO, USA). Chlorin e6 (Ce6) was purchased from Frontier Scientific (Salt Lake City, UT, USA). Icosafluoro-15-crown-5-ether (PFC) was purchased from Tokyo Chemical Industry Co., LTD. (Tokyo, Japan). SY-Glyster CR-310 was kindly provided by Sakamoto Yakuhin Kogyo Co. (Osaka, Japan). 4T1 breast cancer cells were obtained from the American Type Culture Collection (ATCC; Rockville, MD, USA). LIVE/DEAD™ viability/cytotoxicity assay kits, singlet oxygen sensor green reagent (SOSG), and CellROX™ Green reagent were purchased from Thermo Fisher Scientific (Waltham, MA, USA). Anti–HIF–1α primary and Alexa Fluor®-488-conjugated goat anti-rabbit secondary antibodies were purchased from Abcam (Cambridge, MA, USA). *In situ* cell death detection (terminal deoxynucleotidyl transferase dUTP nick end labeling: TUNEL) assay kits were purchased from Roche Diagnostics GmbH (Mannheim, Germany). Hypoxyprobe™-1 Plus kits were obtained from Hypoxyprobe Inc. (Burlington, MA, USA). All other reagents were obtained from Sigma-Aldrich unless otherwise indicated.

4.2. Animals

Animals were cared for in accordance with the National Institutes of Health's Guide for the Care and Use of Laboratory Animals. Protocols were also approved by the Institutional Animal Care and Use Committee (IACUC) of Sungkyunkwan University (IACUC number: 202106301, approval date 22 July 2021). BALB/c *nu/nu* mice (male, 6-weeks-old) were purchased from ORIENT BIO (Seongnam, R. O. Korea). Mice were kept in microisolator cages on individually ventilated cage racks, with unrestricted access to an autoclaved standard rodent diet (LabDiet 5008, Purina, St. Louis, MO, USA) and a 12 h light/dark cycle.

4.3. Synthesis of core UCNPs for red emission

Core UCNPs (~30 nm) were fabricated by slight modification of a previously described procedure [27]. Briefly, $Er(CH_3CO_2)_3$ (6 mmol) in 12 mL methanol was added to a round bottom flask containing 24 mL oleic acid (OA) and 90 mL octadecene (ODE). Methanol was evaporated at 110 °C under vacuum for 25 min, and the reaction temperature was maintained at 150 °C for 1 h under argon flow to obtain a clear solution. After cooling, a methanol solution containing NH_4F (24 mmol) and NaOH (15 mmol) was added slowly to the reaction mixture vessel and kept at 48 °C for 30 min. After removing methanol, the vessel was heated to 308 °C at a rate of 10 °C/min and maintained at this temperature for 90 min under an argon atmosphere. The mixture was cooled to 50 °C, and then 20 mL aliquots of the mixture were mixed with an equal volume of acetone to precipitate the UCNPs. The resulting suspensions were centrifuged at 6554 g for 10 min. Pellets were redispersed in a mixture of OA (6 mL) and ODE (15 mL) to remove impurities as a washing step, and the suspension was further precipitated by the addition of 21 ml acetone. After centrifugation (6554 g for 10 min), pellets were finally collected

and redispersed in 5 ml cyclohexane. Dispersed UCNPs were centrifuged at 1000 g for 5 min to remove large particles. Finally, supernatants containing fine UCNPs (~25 nm) were harvested and stored at 4 °C for further experiments.

4.4. Synthesis and characterization of core@shell UCNPs for red emission

Core@shell ($NaErF_4$@$NaLuF_4$) UCNPs were prepared by slight modification of a procedure described previously. Briefly, $Lu(CH_3CO_2)_3$ (3 mmol) in 7.5 mL methanol was added to a round bottom flask containing 24 mL OA and 90 mL ODE. Methanol was evaporated at 110 °C under vacuum for 30 min, and the temperature was kept at 150 °C for 1 h under argon flow to obtain a clear solution. After cooling, as-synthesized core UCNPs (300 mg) in cyclohexane were added to the solution, and the solution was heated to 110 °C for 30 min under vacuum to remove cyclohexane. The temperature was decreased to 44 °C prior to slowly adding NH_4F (12 mmol) and NaOH (7.5 mmol) in methanol. After a 30 min incubation period at 48 °C, methanol was evaporated using the process described above. The reaction vessel was heated to 308 °C at a rate of 10 °C/min and maintained at this temperature for 90 min under an argon atmosphere. Pellets were washed and redispersed by the same method described for core UCNPs above. Finally, supernatants containing fine Core@shell UCNPs (~35 nm) were harvested and stored at 4 °C for further experiments.

4.5. Synthesis and characterization of core@shell UCNPs for green/red emission

The conventional core@shell ($NaYF_4$: Yb, Nd, Er@$NaLuF_4$) UCNPs was synthesized to compare with $NaErF_4$@$NaLuF_4$ in terms of emission spectrophotometric pattern at the 808 nm excitation wavelength. For the core structure, 6 mmol each of $Y(CH_3CO_2)_3$, $Yb(CH_3CO_2)_3$, $Er(CH_3CO_2)_3$, and $Nd(CH_3CO_2)_3$ [by molar ratio, 68.5% Y, 30% Yb, 0.5% Er, 1% Nd] was dissolved in 10 mL methanol. For the shell structure, 2 mmol of each $Y(CH_3CO_2)_3$ and $Nd(CH_3CO_2)_3$ [by molar ratio, 80% Y, 20% Nd] was dissolved in 4 mL methanol. All relevant synthesis steps are the same as used for synthesis of the $NaErF_4$@$NaLuF_4$ structure described above.

4.6. Preparation of polyacrylic acid-coated core@shell ($NaErF_4$@$NaLuF_4$) UCNPs

Five milliliters of polyacrylic acid (PAA) in ethanol (40 mg/mL) was added to 5 mL of core@shell UCNPs in chloroform (20 mg/mL) and stirred overnight at room temperature. This solution was then centrifuged for 30 min at 14,500 rpm, and PAA-coated-pellets were washed three times with ethanol. Resulting samples were redispersed in PBS (10 mM) and kept at 4 °C.

4.7. Characterization of core@shell UCNPs

Particle sizes of a series of UCNPs were determined by dynamic light scattering (DLS) (Zetasizer Nano-S90, Malvern Instruments Ltd., Worcestershire, UK) at a 90° scattering angle, and particle sizes (mean ± sd) of representative UCNPs from TEM images were also calculated using OriginPro® software (OriginLab®). Irradiation by an 808 nm laser (Laserlab CO, Gyeonggi-do, R. O. Korea) was used to identify the fluorescence emission of UCNPs. Morphology of Core@shell UCNPs was examined by ultrahigh-resolution analytical electron microscopy (HR-TEM) (JEM-3010, JEOL Ltd., Tokyo, Japan). Element composition of materials was captured by TEM and energy dispersive X-ray spectroscopy (EDS; JEM-ARM200F, JEOL Ltd., Tokyo, Japan). Crystal structures of core and core@shell nanoparticles were confirmed by X-ray powder diffraction (XRD) using a D8 ADVANCE system with Davinci (Bruker AXS GmbH, Karlsruhe, Germany) equipped with Cu Ka radiation and a high speed LynxEye detector. Samples were analyzed over the 2θ range of 5–65° with 0.02° increments at a rate of 6°/min. Upconversion emission spectra were collected over the range of 380–780 nm using a photoluminescence spectrophotometer (FLS100, Edinburgh Instruments, UK) at the 808 nm excitation wavelength.

4.8. Preparation of hemoglobin microgels

Hemoglobin microgels (μGels) were fabricated by slight modification of Shirasu porous glass (SPG) membrane emulsification [53–55]. Briefly, w/o emulsions containing different concentrations of Hb/BSA (10/6%, 6/10%, and 0/16% (w/v) in distilled water (DW) were prepared using SPG membranes with a pore size of 3 μm. Dispersed and continuous phases were 3 mL mixture solutions of Hb/BSA (300/180, 180/300, and 0/480 mg, respectively) and 150 mL kerosene with 2%. An internal pressure type micro kit (MCTech, Shihung, R. O. Korea) was used for membrane emulsification. The dispersed phase containing hemoglobin or albumin was passed through the pores of a long tube-shaped SPG membrane by nitrogen gas-driven pressure, and the extruded micro-sized droplets were emulsified in oil phase solution by stirring at 220 rpm to induce the formation of hemoglobin microgels. To synthesize UCNP-loaded Hb microgels, Hb, BSA, and PAA-coated core@shell UCNPs (180, 300 and 120 mg, respectively) were included in the dispersed phase and emulsified by the same procedure described above.

The resulting w/o emulsion containing Hb/BSA/UCNP liquid microdroplets was mixed with 3 mL 50% glutaraldehyde solution (final concentration of 1.0 v/v%) and stirred at 600 rpm for 3 h for cross-linking. The reaction was quenched by adding milled glycine (final concentration; 0.05 M) and allowed to continue for 30 min. The resulting mixture containing Hb microgels was centrifuged at 6108 g and washed 3 times with 10 mM PBS containing 0.02% Tween 80 and 50% ethanol. Pellets were finally washed with DW, and the resulting Hb μGel solution was briefly filtered through a 10–15 μm mesh strainer to remove aggregated particles and further lyophilized with 3% d-(+)-trehalose dihydrate to prevent aggregation during the lyophilization step. To incorporate Ce6, a portion (20 mg) of the freeze-dried Hb μGel with dissolved UCNPs was mixed with 4 mL of Ce6 (100 μg/mL) dissolved in a 1:9 mixed solution of DMSO and DW. The resulting Ce6/Er@Lu UCNP-loaded Hb μGels were briefly centrifuged at 4000 rpm for 3 min. Supernatant was removed, and the μGels were washed three time with PBS and stored at 4 °C for further experiments.

4.9. Characterization of hemoglobin microgels

UCNP-loaded Hb μGels were carefully characterized using various analytical instruments. Two main components of UCNP-loaded Hb μGels, namely Hb and BSA (fluorescein isothiocynate (FITC) modified), were visualized by confocal laser scanning microscopy (CLSM; LSM510, Carl Zeiss, Jena, Germany) using excitation/emission wavelengths of 549/628 and 495/519 nm, respectively. Surface morphology and red fluorescence of Hb μGels were examined by optical/fluorescence microscopy (ECLIPSE Ts2-FL, Nikon corp., Tokyo, Japan) and Field emission scanning electron microscopy (FE-SEM) (JSM7500F, JEOL Ltd, Tokyo, Japan). Cross-sectional UCNP-loaded Hb μGel samples were prepared by focused ion beam (FIB) (JIB-4601 F, JEOL Ltd, Tokyo, Japan) and analyzed by FE-SEM and high-resolution transmission electron microscopy (HR-TEM) (JEM-3010, JEOL Ltd, Tokyo, Japan), respectively. μGel samples were lyophilized for 2 days before analysis. Additionally, UCNP-loaded Hb μGels containing chlorin e6 were visualized by CLSM.

4.10. In vitro and in vivo evaluation of the photothermal effect of hemoglobin microgels

A thermal imaging camera was used to examine the photothermal effect of Hb μGels *in vitro* and *in vivo*. Hb μGel samples (Hb/BSA feed weight ratios: 10:6, 6:10, and 0:16) were placed in 0.5 mL tubes (Costar,

0.5 mL individual PCR tubes). Each microtube was irradiated with 808 nm laser (1.5 W/cm^2) for 20 min. Surface temperature was monitored every minute. Mild hyperthermia (41–42 °C) was induced by 3 min alternation of on/off 808 nm light irradiation. To obtain photothermal images *in vivo*, PBS or Hb μGel samples were injected intratumorally into 4T1-tumor bearing mice and tumor regions were irradiated with 808-nm laser (1.5 W/cm^2) for 15 min. The diameter of the laser spot was adjusted to 1 cm. The following equation was used to calculate the laser output power: laser output power (W) = laser fluence (W/cm^2) × spot area (cm^2). Temperature increases and thermal images were monitored every minute using a thermographic camera (FLIR E85). Additionally, fluorescence and thermal images of Hb μGel samples mounted on a plate (1 cm diameter) were obtained by thermographic camera and FOBI *in vivo* imaging equipment (NeoScience, Suwon, Korea), respectively.

4.11. Spectrophotometric analysis of hemoglobin microgels

Circular dichroism (CD) spectra from DW, Hb, BSA, and various Hb μGels containing UCNPs were recorded at a concentration of 1 mg/mL in DW using a dichroism spectropolarimeter (J-1500, Jasco International Co., Ltd., USA). The far UV region was scanned between 190 nm and 260 nm. UV-VIS absorption patterns of Hb μGels were monitored in the wavelength range of 350–550 nm using UV-VIS spectrophotometry according to the presence of ascorbic acid and/or oxygen.

4.12. Preparation of perfluorocarbon (PFC)-based albumin nanoemulsion (PFC/BSA-NE) and PFC/UCNP-loaded Hb_0 μGels

A portion (250 μL) of icosafluoro-15-crown-5-ether (PFC) was added to 2.5 mL PBS solution containing 40 mg BSA. The mixture was then placed in an ice bath and ultrasonicated for 200 s at 20% amplitude (operation 8 s, interval 2 s). The obtained emulsion was centrifuged (8000 rpm, 3 min) and redispersed in 0.5 mL PBS. Separately, 0.5 mL of PFC/BSA-NE (40 mg and 250 μL BSA and PFC, respectively) was mixed with 2.5 mL dispersed phase containing 440 mg BSA and 120 mg UCNPs. Hb_0 μGels were fabricated using the same procedure described above for SPG membrane emulsification and microgel hardening.

4.13. Singlet oxygen ($^1O_2$) generation by UCNP-loaded Hb μGel

Singlet oxygen generation from UCNP-loaded Hb μGels was detected using singlet oxygen sensor green (SOSG) reagent. Samples were divided into six groups (I) PBS; (II) Hb_6 μGel (Hb:BSA = 6:10) + N_2 for hypoxia; (III) Hb_6 μGel + O_2 for oxygenation; (IV) Hb_6 μGel + ascorbic acid + O_2; (V) PFC/BSA-NE-loaded Hb_0 μGel + O_2 + US(+); (VI) PFC/BSA-NE-loaded Hb_0 μGel + O_2 + US(−). Hypoxic samples were placed in a 48-well plate pre-filled with a hypoxic solution (DW:DMSO = 9:1, hypoxic chamber overnight). Hypoxia was achieved by incubating 48-well plates in a hypoxic gas stream (5% CO_2:95% N_2 on a volume basis). Oxygenated samples were prepared under oxygen gas flow for 20 min. All samples were mixed with SOSG reagent (final concentration 5 μM) and quickly added to hypoxic solution in the wells of a 48-well plate using a needle syringe through an adhesive plate cover. Each well was irradiated by 808-nm laser (1.5 W/cm^2) for 60 min. While irradiating the sample wells with the laser for 60 min, a 100 μL aliquot of each sample was collected every 10 min. A multi-mode microplate reader was used to measure the intensity of the green fluorescence (excitation and emission wavelengths of 485 and 538 nm, respectively) emitted from SOSG induced by $^1O_2$ production. Mild ultrasound (1 MHz, 3 W/cm^2) was applied to sample group V. All samples were transferred to a black 96-well plate for fluorescence detection. The SOSG fluorescence signal was visualized using an FOBI *in vivo* imaging system (NeoScience, Suwon, Korea).

4.14. Measurement of O_2 release

Oxygen concentration (ppm; mg/L) in aqueous solutions purged with N_2 gas was determined by oxygen meter (PreSens, Regensburg, Germany) before and after adding the following samples: (I) Hb_6 μGel (Hb:BSA = 6:10) + N_2 (nitrogen gas) for hypoxia; (II) Hb_6 μGel + O_2 for oxygenation; (III) Hb_6 μGel + ascorbic acid + O_2; (IV) PFC/BSA-NE-loaded Hb_0 μGel + O_2 + US(+); (V) PFC/BSA-NE-loaded Hb_0 μGel + O_2 + US(−). The oxygen concentration of PFC/BSA-NE-loaded Hb_0 μGel was measured with and without ultrasound treatment (1 MHz, 3 W/cm^2). Oxygen content of hypoxic medium in a 200 μL vial was measured for the first 300 s to record hypoxic conditions, samples were added into the vial, and measurements were performed for an additional 300 s. External US treatment was applied to one tube for another 300 s. Oxygen concentrations of all samples were measured for a total of 1500 s. Hypoxic conditions were maintained by N_2 gas purging for 10 min (N_2 flow rate = 0.1 MPa).

4.15. Fluorescence visualization by CLSM of Hb μGel & 4T1 cell spheroids

4T1 cell spheroids were prepared in a V-bottom 96-well plate (Shimadzu, Tokyo, Japan). 4T1 cells (100 μL, 4 × 10^4 cells/mL) were seeded into each well and cultured for 72 h. Spheroids were transferred to 96-well plates with a U-shaped bottom, and the media was replenished with 100 μL DMEM medium containing 1% FBS and 1% penicillin/streptomycin (P/S/; Corning, NY, USA). 4T1 cell spheroids were plated in each well of an 8-well chamber (Ibidi, Martinsried, Germany) and stained with Hoechst. Spheroids were mixed with Hb_6 μGels and visualized by CLSM (Carl Zeiss, Jena, Germany) to observe the effects of the microgels on the spheroids.

4.16. HIF-1α visualization of 3D 4T1 cell spheroids

Prepared 4T1 cell spheroids were treated with (I) PBS under normoxic or hypoxic conditions, (II) Hb_6 μGel under normoxic or hypoxic conditions, (III) Hb_6 μGel + ascorbic acid + O_2 in sealed hypoxic media plate wells; and (IV) PFC/BSA-NE-loaded Hb_0 μGel + O_2 + US(+) in sealed hypoxic media plate wells. Spheroids were fixed in 4% formaldehyde for 10 min before incubation in 0.1% Triton X-100 for 5 min. Spheroids were then incubated with 1% BSA and PBS with 0.2% Tween 80 containing glycine (22.5 mg/mL) for 1 h to block nonspecific binding of antibodies. Spheroids were treated with a 1/50 dilution of anti–HIF–1α antibody-Alexa Fluor 488 and incubated overnight at 4 °C (Abcam, Cambridge, USA), and nuclei were stained with Hoechst. Samples were observed using CLSM.

4.17. ROS deep assay

Prepared 4T1 cell spheroids were treated with (I) UCNP-loaded Hb_6 μGel + Ce6 under normoxic conditions with or without 808 nm laser irradiation, (II) UCNP-loaded Hb_6 μGel + ascorbic acid/Ce6 + O_2 in sealed hypoxic media plate wells with or without 808 nm laser irradiation, and (III) UCNPs and PFC/BSA-NE-loaded Hb_0 μGel + Ce6 + O_2 + US(+) in sealed hypoxic media plate wells. Under normoxic and hypoxic conditions, ROS detection was carried out during laser irradiation (wavelength of 808 nm) for 30 min. CellROX® reagent was applied to spheroids at a final concentration of 20 μM, followed by a 30 min incubation at 37 °C. 4T1 cell spheroids were washed three times with PBS and stained with DAPI. CLSM (Carl Zeiss, Jena, Germany) was used to observe the production and distribution of reactive oxygen species (ROS) inside cells.

4.18. In vitro cytotoxicity of 4T1 cell spheroids using the LIVE/DEAD™ assay

First, the photodynamic effect of UCNP-loaded Hb_6 μGels on the viability of cell spheroids was assessed under the following hypoxic conditions: (I) UCNP-loaded Hb_6 μGel + Ce6 with or without 808 nm laser irradiation, (II) UCNP-loaded Hb_6 μGel + ascorbic acid/Ce6 + O_2 in sealed hypoxic media plate wells with or without 808 nm laser irradiation, and (III) UCNP and PFC/BSA-NE loaded Hb_0 μGel + Ce6 + O_2 + US(+) in sealed hypoxic media plate wells with or without 808 nm laser irradiation. Samples were irradiated at 808 nm for 30 min in the dark. Ascorbic acid was added into the Hb_6 μGel, and oxygenation by O_2 purging was conducted for 10 min. For group III, ultrasound (1 MHz, 3 W/cm^2) was applied to wells containing spheroids and microgels before laser irradiation. Additionally, spheroids were treated with (I) PBS and 808 nm laser, (II) UCNP-loaded Hb_0 μGel (20 mg/mL) + Ce6 with or without 808 nm laser irradiation, and (III) Hb_6 μGel (30 mg/mL) with or without 808 nm laser irradiation. These were considered the respective negative control, PDT only, and PTT only groups. Additionally, the following spheroid groups were designated: (I) mild PTT + PDT, (II) mild PTT for target temperature of 41–42 °C, and (iii) strong PTT for a target temperature >48 °C under normoxic conditions. To create these groups, spheroids were treated with (I) UCNP-loaded Hb_6 μGel (20 mg/mL) + ascorbic acid/Ce6 with or without 808 nm laser irradiation (1.5 W/cm^2), (II) Hb_6 μGel (20 mg/mL) with or without 808 nm laser irradiation (1.5 W/cm^2), and (III) Hb_6 μGel (40 mg/mL) with or without 808 nm laser irradiation (1.5 W/cm^2). After laser treatment, spheroids were washed three times with DPBS, and the medium was replenished with fresh 1% FBS and 1% P/S DMEM and placed in a CO_2 chamber overnight. Spheroids were then stained with Calcein-AM (for live cells) and ethidium homodimer-1 (for dead cells). Subsequently, stained cells were observed by CLSM using excitation/emission wavelengths of 494/517 nm for Calcein-AM and 528/617 nm for ethidium homodimer-1, respectively. Hypoxia was achieved by incubation in a hypoxic chamber under a hypoxic gas stream (5% CO_2:95% N_2 on a volume basis). In addition, relevant samples were placed in hypoxic media prior to oxygen generation.

4.19. Evaluation of the in vitro cytotoxicity of Hb μGels

Cytotoxic effects of gels against 4T1 cells (breast cancer cell line) were assessed using a 3-(4,5-dimethylthiazol-2-yl)-2,5-diphenyltetrazolium bromide (MTT)-based assay. 4T1 cells were seeded at 1×10^4 cells/well in 96-well plates and pre-incubated for 24 h in DMEM media containing 10% FBS and 1% P/S. After replacing the cell culture medium with DMEM media, cells were washed twice with DPBS. Cells were treated with the various Hb μGel samples (Hb_0 μGel, Hb_6 μGel, and Hb_{10} μGel: 100 μL) at different concentrations for 4 h μGels were removed from the plates by washing with DPBS. Cell viabilityell viability was analyzed using the MTT assay.

4.20. Visualization of 4T1 cell-xenografted mice injected with UCNP-loaded Hb microgels

The injection site of UCNP-loaded Hb μGels was monitored by computerized tomography (CT; SKY-scan 1076, Broker, USA) at 0, 1, and 7 days. Cy5.5-Hb μGel, which was modified with Cy5.5-NHS (GE Healthcare, Chicago, USA), was injected directly into the tumors of 4T1 cell-xenografted mice, and fluorescence signals were visualized at predetermined times and at wavelengths corresponding to Cy5.5 and hemoglobin using FOBI *in vivo* imaging equipment (NeoScience, Suwon, R. O. Korea). Separately, the major organs (liver, kidney, spleen, lung and heart) of the mouse were exicsed and visualized at 24 h after sacrifice of mice.

4.21. Photoacoustic (PA) imaging to detect oxygen generation

Oxygen levels inside xenografted 4T1 tumors were monitored after injecting various samples using photoacoustic (PA) imaging. When tumors reached ~150 mm^3 in volume, mice were treated with (I) PBS, (II) hypoxic Hb_6 μGel, (III) Hb_0 μGel + PFC + US(−), (IV) Hb_0 μGel + PFC + US(+), and (V) Hb_6 μGel + ascorbic acid + O_2. Tumor oxygenation (as oxyhemoglobin: HbO_2 ratio) was visualized and recorded using a Vevo® LAZR-X Multimodal Imaging System (FujiFilm, VisualSonics Inc., Minato, Tokyo, Japan) set to oxy-hem mode (750 and 850 nm) before injection (−5 min) and at 0, 5, 15, 30, and 60 min after injection. Average oxygen level histograms showed pixel-based oxygen saturation percentages.

4.22. In vivo antitumor efficacy

4T1 cells (100 μL, 2×10^6 cells) were subcutaneously injected into the dorsal flanks of mice. When the volume of the tumors reached 120–150 mm^3, mice were randomly divided into seven groups as follows: G1 - PBS (non-treated); G2 - Hb_6 μGel + 808 nm (+) under a mild temperature (41–42 °C) setting; G3 - Hb_0 μGel (+UCNPs/Ce6) previously treated with nitrogen to maintain a hypoxic state + 808 nm (+) (1.5 W/cm^2 for 20 min); G4 - Hb_6 μGel (+UCNPs/Ce6) + ascorbic acid + O_2 + 808 nm (−); G5 - Hb_0 microgel (+UCNPs/Ce6) + PFC + O_2 + 808 nm (+) + US(+) (60 min); G6 - Hb_{10} μGel (+UCNPs) + 808 nm (+) (1.5 W/cm^2 for 30 min) under strong hyperthermia (>48 °C) and G7 - Hb_6 μGel (+UCNPs/Ce6) + ascorbic acid + O_2 + 808 nm (+) under a mild temperature (41–42 °C) setting. Tumor size was measured every day, and volume (V) was calculated using equation $V = 0.5 \times A \times B^2$, where A is the longest diameter (mm), and B is the shortest diameter (mm). Each sample (50 μL; 20 mg/mL of μGel) was intratumorally injected into a mouse. Body weights of mice in all groups were measured every day. On day 20, mice were sacrificed, and their tumors were excised and photographed (n = 4). For H&E and TUNEL staining, tumors and major organs (liver, kidney, spleen, lung and heart) of all mice were dissected and paraffin sections were prepared. H&E and TUNEL staining were performed according to the manufacturers' protocols, and cells were examined by digital CLSM.

Separately, the G7* mice (n = 3), which were treated same with G7 but cared until day 30, were carefully monitored in terms of tumor volume and body weight. Additional two groups of mice (each n = 4), H1 and H2, were treated with (i) only 808 nm laser irradiation alone (1.5 W/cm^2 for 60 min) and (ii) Hb_{10} μGel (+UCNPs without Ce6) with 808 nm laser irradiation at a mild temperature setting (41–42 °C). Their tumor volumes and body weights were measured.

4.23. In vivo hypoxia assay

The *in vivo* hypoxia assay was performed by slight modification of a protocol described previously. Mice with ~300 mm^3 tumors were treated with a fixed concentration of one of the μGels and then intraperitoneally injected with pimonidazole hydrochloride (200 mg/kg) (Hypoxyprobe™-1 Plus Kit; Hypoxyprobe Inc. Burlington, MA, USA). After 90 min, tumors were surgically resected for frozen sectioning. For immunofluorescence staining, paraffin sections of tumors were prepared and treated with mouse anti-pimonidazole primary antibody (dilution 1:200, Hypoxyprobe Inc.) and Alexa 488-conjugated goat anti-mouse secondary antibody (dilution 1:200, Jackson Inc.) according to the kit instructions. Nuclei were stained with DAPI (dilution 1:5000, Invitrogen, Waltham, MA, USA). Slices were observed by CLSM.

CRediT authorship contribution statement

Hanju Kim: Data curation, Methodology, Investigation, Writing – original draft. **Johyun Yoon:** Data curation, Methodology. **Hwang Kyung Kim:** Data curation, Methodology. **Woo Tak Lee:** Data curation,

Investigation. **Nguyen Thi Nguyen:** Data curation. **Xuan Thien Le:** Data curation, Investigation. **Eun-Hee Lee:** Data curation, Methodology. **Eun Seong Lee:** Supervision. **Kyung Taek Oh:** Supervision. **Han-Gon Choi:** Supervision. **Yu Seok Youn:** Conceptualization, Writing – original draft, Writing – review & editing, Supervision, Project administration, Funding acquisition.

Declaration of competing interest

The authors have no conflicts of interest to declare.

Acknowledgments

This work was supported by a National Research Foundation of Korea (NRF) grants funded by the Korean government (No. NRF-2019R1A5A2027340) and the Bio & Medical Technology Development Program of the National Research Foundation (NRF) funded by the Korean government (MSIT) (No. NRF-2022M3A9G8017220).

Appendix A. Supplementary data

Supplementary data to this article can be found online at https://doi.org/10.1016/j.bioactmat.2022.09.020.

References

[1] A.I. Alayash, Oxygen therapeutics: can we tame haemoglobin? Nat. Rev. Drug Discov. 3 (2) (2004) 152–159, https://doi.org/10.1038/nrd1307.
[2] M.M. Jansman, L. Hosta-Rigau, Recent and prominent examples of nano-and microarchitectures as hemoglobin-based oxygen carriers, Adv. Colloid Interface Sci. 260 (2018) 65–84, https://doi.org/10.1016/j.cis.2018.08.006.
[3] Z. Tao, P.P. Ghoroghchian, Microparticle, nanoparticle, and stem cell-based oxygen carriers as advanced blood substitutes, Trends Biotechnol. 32 (9) (2014) 466–473, https://doi.org/10.1016/j.tibtech.2014.05.001.
[4] R.M. Winslow, MP4, a new nonvasoactive polyethylene glycol–hemoglobin conjugate, Artif. Organs 28 (9) (2004) 800–806, https://doi.org/10.1111/j.1525-1594.2004.07392.x.
[5] P. Cabrales, Examining and mitigating acellular hemoglobin vasoactivity, Antioxid. redox signal. 18 (17) (2013) 2329–2341, https://doi.org/10.1089/ars.2012.4922.
[6] K.D. Vandegriff, R.M. Winslow, Hemospan: design principles for a new class of oxygen therapeutic, Artif. Organs 33 (2) (2009) 133–138, https://doi.org/10.1111/j.1525-1594.2008.00697.x.
[7] M. Pilarek, Liquid perfluorochemicals as flexible and efficient gas carriers applied in bioprocess engineering: an updated overview and future prospects, Chem. Process Eng. 35 (4) (2014) 463–487, https://doi.org/10.2478/cpe-2014-0035.
[8] S. Sadrzadeh, E. Graf, S.S. Panter, P. Hallaway, J. Eaton, Hemoglobin. A biologic fenton reagent, J. Biol. Chem. 259 (23) (1984) 14354–14356, https://doi.org/10.1016/S0021-9258(17)42604-4.
[9] B.R. Van Dyke, P. Saltman, Hemoglobin: a mechanism for the generation of hydroxyl radicals, Free Radic. Biol. Med. 20 (7) (1996) 985–989, https://doi.org/10.1016/0891-5849(95)02186-8.
[10] L. Duan, X. Yan, A. Wang, Y. Jia, J. Li, Highly loaded hemoglobin spheres as promising artificial oxygen carriers, ACS Nano 6 (8) (2012) 6897–6904, https://doi.org/10.1021/nn301735u.
[11] W. Tang, Z. Zhen, M. Wang, H. Wang, Y.J. Chuang, W. Zhang, G.D. Wang, T. Todd, T. Cowger, H. Chen, Red blood cell-facilitated photodynamic therapy for cancer treatment, Adv. Funct. Mater. 26 (11) (2016) 1757–1768, https://doi.org/10.1002/adfm.201504803.
[12] N. Doshi, A.S. Zahr, S. Bhaskar, J. Lahann, S. Mitragotri, Red blood cell-mimicking synthetic biomaterial particles, Proc. Natl. Acad. Sci. USA 106 (51) (2009) 21495–21499, https://doi.org/10.1073/pnas.0907127106.
[13] S. Kizaka-Kondoh, M. Inoue, H. Harada, M. Hiraoka, Tumor hypoxia: a target for selective cancer therapy, Cancer Sci. 94 (12) (2003) 1021–1028, https://doi.org/10.1111/j.1349-7006.2003.tb01395.x.
[14] J.M. Brown, W.R. Wilson, Exploiting tumour hypoxia in cancer treatment, Nat. Rev. Cancer 4 (6) (2004) 437–447, https://doi.org/10.1038/nrc1367.
[15] S. Rey, L. Schito, M. Koritzinsky, B.G. Wouters, Molecular targeting of hypoxia in radiotherapy, Adv. Drug Deliv. Rev. 109 (15) (2017) 45–62, https://doi.org/10.1016/j.addr.2016.10.002.
[16] C.-C. Huang, W.-T. Chia, M.-F. Chung, K.-J. Lin, C.-W. Hsiao, C. Jin, W.-H. Lim, C.-C. Chen, H.-W. Sung, An implantable depot that can generate oxygen in situ for overcoming hypoxia-induced resistance to anticancer drugs in chemotherapy, J. Am. Chem. Soc. 138 (16) (2016) 5222–5225, https://doi.org/10.1021/jacs.6b01784.
[17] G. Yang, L. Xu, Y. Chao, J. Xu, X. Sun, Y. Wu, R. Peng, Z. Liu, Hollow MnO 2 as a tumor-microenvironment-responsive biodegradable nano-platform for combination therapy favoring antitumor immune responses, Nat. Commun. 8 (1) (2017) 1–13, https://doi.org/10.1038/s41467-017-01050-0.
[18] H. Chen, J. Tian, W. He, Z. Guo, H2O2-activatable and O2-evolving nanoparticles for highly efficient and selective photodynamic therapy against hypoxic tumor cells, J. Am. Chem. Soc. 137 (4) (2015) 1539–1547, https://doi.org/10.1021/ja511420n.
[19] Y. Cheng, H. Cheng, C. Jiang, X. Qiu, K. Wang, W. Huan, A. Yuan, J. Wu, Y. Hu, Perfluorocarbon nanoparticles enhance reactive oxygen levels and tumour growth inhibition in photodynamic therapy, Nat. Commun. 6 (1) (2015) 1–8, https://doi.org/10.1038/ncomms9785.
[20] X. Song, L. Feng, C. Liang, K. Yang, Z. Liu, Ultrasound triggered tumor oxygenation with oxygen-shuttle nanoperfluorocarbon to overcome hypoxia-associated resistance in cancer therapies, Nano Lett. 16 (10) (2016) 6145–6153, https://doi.org/10.1021/acs.nanolett.6b02365.
[21] P. Prasad, C.R. Gordijo, A.Z. Abbasi, A. Maeda, A. Ip, A.M. Rauth, R.S. DaCosta, X. Y. Wu, Multifunctional albumin–MnO2 nanoparticles modulate solid tumor microenvironment by attenuating hypoxia, acidosis, vascular endothelial growth factor and enhance radiation response, ACS Nano 8 (4) (2014) 3202–3212, https://doi.org/10.1021/nn405773r.
[22] S. Gao, G. Wang, Z. Qin, X. Wang, G. Zhao, Q. Ma, L. Zhu, Oxygen-generating hybrid nanoparticles to enhance fluorescent/photoacoustic/ultrasound imaging guided tumor photodynamic therapy, Biomaterials 112 (2017) 324–335, https://doi.org/10.1016/j.biomaterials.2016.10.030.
[23] C. Lee, K. Lim, S.S. Kim, E.S. Lee, K.T. Oh, H.-G. Choi, Y.S. Youn, Chlorella-gold nanorods hydrogels generating photosynthesis-derived oxygen and mild heat for the treatment of hypoxic breast cancer, J. Contr. Release 294 (28) (2019) 77–90, https://doi.org/10.1016/j.jconrel.2018.12.011.
[24] L. Chen, W. Wang, J. Tian, F. Bu, T. Zhao, M. Liu, R. Lin, F. Zhang, M. Lee, D. Zhao, Imparting multi-functionality to covalent organic framework nanoparticles by the dual-ligand assistant encapsulation strategy, Nat. Commun. 12 (1) (2021) 1–10, https://doi.org/10.1038/s41467-021-24838-7.
[25] L. Chen, T. Zhao, M. Zhao, W. Wang, C. Sun, L. Liu, Q. Li, F. Zhang, D. Zhao, X. Li, Size and charge dual-transformable mesoporous nanoassemblies for enhanced drug delivery and tumor penetration, Chem. Sci. 11 (10) (2020) 2819–2827, https://doi.org/10.1039/C9SC06260B.
[26] P. Avci, A. Gupta, M. Sadasivam, D. Vecchio, Z. Pam, N. Pam, M.R. Hamblin, Low-level laser (light) therapy (LLLT) in skin: stimulating, healing, restoring, Semin. Cutan. Med. Surg. 32 (1) (2013) 41–52.
[27] S.S. Lucky, K.C. Soo, Y. Zhang, Nanoparticles in photodynamic therapy, Chem. Rev. 115 (4) (2015) 1990–2042, https://doi.org/10.1021/cr5004198.
[28] W.T. Lee, J. Yoon, S.S. Kim, H. Kim, N.T. Nguyen, X.T. Le, E.S. Lee, K.T. Oh, H.-G. Choi, Y.S. Youn, Combined Antitumor Therapy Using In Situ Injectable Hydrogels Formulated with Albumin Nanoparticles Containing Indocyanine Green, Chlorin e6, and Perfluorocarbon in Hypoxic Tumors, Pharmaceutics 14 (1) (2022) 148, https://doi.org/10.3390/pharmaceutics14010148.
[29] K. Lim, H.K. Kim, X.T. Le, N.T. Nguyen, E.S. Lee, K.T. Oh, H.-G. Choi, Y.S. Youn, Highly red light-emitting erbium-and lutetium-doped core-shell upconverting nanoparticles surface-modified with PEG-folic acid/TCPP for suppressing cervical cancer HeLa cells, Pharmaceutics 12 (11) (2020) 1102, https://doi.org/10.3390/pharmaceutics12111102.
[30] S. He, N.J. Johnson, V.A. Nguyen Huu, Y. Huang, A. Almutairi, Leveraging spectral matching between photosensitizers and upconversion nanoparticles for 808 nm-activated photodynamic therapy, Chem. Mater. 30 (12) (2018) 3991–4000, https://doi.org/10.1021/acs.chemmater.7b04700.
[31] Z. Gu, L. Yan, G. Tian, S. Li, Z. Chai, Y. Zhao, Recent advances in design and fabrication of upconversion nanoparticles and their safe theranostic applications, Adv. Mater. 25 (28) (2013) 3758–3779, https://doi.org/10.1002/adma.201301197.
[32] S. Wilhelm, Perspectives for upconverting nanoparticles, ACS Nano 11 (11) (2017) 10644–10653, https://doi.org/10.1021/acsnano.7b07120.
[33] D. Jaque, L.M. Maestro, B. del Rosal, P. Haro-Gonzalez, A. Benayas, J. Plaza, E. M. Rodríguez, J.G. Solé, Nanoparticles for photothermal therapies, Nanoscale 6 (16) (2014) 9494–9530, https://doi.org/10.1039/C4NR00708E.
[34] C. Song, A. Shakil, J. Osborn, K. Iwata, Tumour oxygenation is increased by hyperthermia at mild temperatures, Int. J. Hyperther. 12 (3) (1996) 367–373, https://doi.org/10.3109/02656739609022525.
[35] K. Okajima, R.J. Griffin, K. Iwata, A. Shakil, C.W. Song, Tumor oxygenation after mild-temperature hyperthermia in combination with carbogen breathing: dependence on heat dose and tumor type, Radiat. Res. 149 (3) (1998) 294–299, https://doi.org/10.2307/3579963.
[36] A. Shakil, J.L. Osborn, C.W. Song, Changes in oxygenation status and blood flow in a rat tumor model by mild temperature hyperthermia, Int. J. Radiat. Oncol. Biol. Phys. 43 (4) (1999) 859–865, https://doi.org/10.1016/s0360-3016(98)00516-1.
[37] P. Wust, B. Hildebrandt, G. Sreenivasa, B. Rau, J. Gellermann, H. Riess, R. Felix, P. Schlag, Hyperthermia in combined treatment of cancer, Lancet Oncol. 3 (8) (2002) 487–497, https://doi.org/10.1016/s1470-2045(02)00818-5.
[38] F.K. Storm, Clinical hyperthermia and chemotherapy, Radiol. Clin. 27 (3) (1989) 621–627.
[39] P.T.T. Pham, X.T. Le, H. Kim, H.K. Kim, E.S. Lee, K.T. Oh, H.-G. Choi, Y.S. Youn, Indocyanine green and curcumin Co-loaded nano-fireball-like albumin nanoparticles based on near-infrared-induced hyperthermia for tumor ablation, Int. J. Nanomed. 15 (2020) 6469, https://doi.org/10.2147/IJN.S262690.
[40] C. Lee, H.S. Hwang, S. Lee, B. Kim, J.O. Kim, K.T. Oh, E.S. Lee, H.G. Choi, Y. S. Youn, Rabies virus-inspired silica-coated gold nanorods as a photothermal therapeutic platform for treating brain tumors, Adv. Mater. 29 (13) (2017), 1605563, https://doi.org/10.1002/adma.201605563.
[41] L. Zhang, D. Wang, K. Yang, D. Sheng, B. Tan, Z. Wang, H. Ran, H. Yi, Y. Zhong, H. Lin, Mitochondria-targeted artificial “nano-RBCs” for amplified synergistic

cancer phototherapy by a single NIR irradiation, Adv. Sci. 5 (8) (2018), 1800049, https://doi.org/10.1002/advs.201800049.
[42] S. Park, H. Kim, S.C. Lim, K. Lim, E.S. Lee, K.T. Oh, H.-G. Choi, , YSJJoCR, Youn, Gold nanocluster-loaded hybrid albumin nanoparticles with fluorescence-based optical visualization and photothermal conversion for tumor detection/ablation, J. Contr. Release 304 (28) (2019) 7–18, https://doi.org/10.1016/j.jconrel.2019.04.036.
[43] X. Li, R. Wang, F. Zhang, D. Zhao, Engineering homogeneous doping in single nanoparticle to enhance upconversion efficiency, Nano Lett. 14 (6) (2014) 3634–3639, https://doi.org/10.1021/nl501366x.
[44] M.D. Wisser, S. Fischer, C. Siefe, A.P. Alivisatos, A. Salleo, J.A. Dionne, Improving quantum yield of upconverting nanoparticles in aqueous media via emission sensitization, Nano Lett. 18 (4) (2018) 2689–2695, https://doi.org/10.1021/acs.nanolett.8b00634.
[45] S. Fischer, N.D. Bronstein, J.K. Swabeck, E.M. Chan, A.P. Alivisatos, Precise tuning of surface quenching for luminescence enhancement in core–shell lanthanide-doped nanocrystals, Nano Lett. 16 (11) (2016) 7241–7247, https://doi.org/10.1021/acs.nanolett.6b03683.
[46] R. Singh, G. Dumlupinar, S. Andersson-Engels, S. Melgar, Emerging applications of upconverting nanoparticles in intestinal infection and colorectal cancer, Int. J. Nanomed. 14 (2019) 1027–1038, https://doi.org/10.2147/IJN.S188887.
[47] B. Chen, F. Wang, Emerging frontiers of upconversion nanoparticles, Trends Chem 2 (5) (2020) 427–439, https://doi.org/10.1016/j.trechm.2020.01.008.
[48] G. Chen, H. Qiu, P.N. Prasad, X. Chen, Upconversion nanoparticles: design, nanochemistry, and applications in theranostics, Chem. Rev. 114 (10) (2014) 5161–5214, https://doi.org/10.1021/cr400425h.
[49] D. Chen, M. Xu, M. Ma, P. Huang, Effects of Er 3+ spatial distribution on luminescence properties and temperature sensing of upconverting core–shell nanocrystals with high Er 3+ content, Dalton Trans. 46 (44) (2017) 15373–15385, https://doi.org/10.1039/C7DT02915B.
[50] L. Zhao, J. Peng, Q. Huang, C. Li, M. Chen, Y. Sun, Q. Lin, L. Zhu, F. Li, Near-infrared photoregulated drug release in living tumor tissue via yolk-shell upconversion nanocages, Adv. Funct. Mater. 24 (3) (2014) 363–371, https://doi.org/10.1002/adfm.201302133.
[51] P. Ramasamy, J. Kim, Combined plasmonic and upconversion rear reflectors for efficient dye-sensitized solar cells, Chem. Commun. 50 (7) (2014) 879–881, https://doi.org/10.1039/C3CC47290F.
[52] S. Wang, K. Han, S. Ma, X. Qi, L. Guo, X. Li, Blood cells as supercarrier systems for advanced drug delivery, Med. Drug Discov. 13 (2022), 100119, https://doi.org/10.1016/j.medidd.2021.100119.
[53] Y.T. Lai, M. Sato, S. Ohta, K. Akamatsu, S.-i. Nakao, Y. Sakai, T. Ito, Preparation of uniform-sized hemoglobin–albumin microspheres as oxygen carriers by Shirasu porous glass membrane emulsification technique, Colloids Surf. B Biointerfaces 127 (2015) 1–7, https://doi.org/10.1016/j.colsurfb.2015.01.018.
[54] Y.T. Lai, S. Ohta, K. Akamatsu, S.i. Nakao, Y. Sakai, T. Ito, Size-dependent interaction of cells and hemoglobin–albumin based oxygen carriers prepared using the SPG membrane emulsification technique, Biotechnol. Prog. 31 (6) (2015) 1676–1684, https://doi.org/10.1002/btpr.2170.
[55] S. Ohta, K. Hashimoto, X. Fu, M. Kamihira, Y. Sakai, T. Ito, Development of human-derived hemoglobin–albumin microspheres as oxygen carriers using Shirasu porous glass membrane emulsification, J. Biosci. Bioeng. 126 (4) (2018) 533–539, https://doi.org/10.1016/j.jbiosc.2018.04.017.
[56] S.F. Himmelstoß, T. Hirsch, Long-term colloidal and chemical stability in aqueous media of NaYF4-type upconversion nanoparticles modified by ligand-exchange, Part. Part, Syst. Charact. 36 (10) (2019), 1900235, https://doi.org/10.1002/ppsc.201900235.
[57] H. Keum, D. Yoo, S. Jon, Photomedicine based on heme-derived compounds, Adv. Drug Deliv. Rev. 182 (2022), 114134, https://doi.org/10.1016/j.addr.2022.114134.
[58] J.F. Lovell, C.S. Jin, E. Huynh, H. Jin, C. Kim, J.L. Rubinstein, W.C. Chan, W. Cao, L.V. Wang, G. Zheng, Porphysome nanovesicles generated by porphyrin bilayers for use as multimodal biophotonic contrast agents, Nat. Mater. 10 (4) (2011) 324–332, https://doi.org/10.1038/nmat2986.
[59] C. Lee, K. Lim, S.S. Kim, E.S. Lee, K.T. Oh, H.-G. Choi, Y.S. Youn, Near infrared light-responsive heat-emitting hemoglobin hydrogels for photothermal cancer therapy, Colloids Surf. B Biointerfaces 176 (2019) 156–166, https://doi.org/10.1016/j.colsurfb.2018.12.070.
[60] C. Heckl, A. Lang, A. Rühm, R. Sroka, T. Duffield, M. Vogeser, M. Paal, Spectrophotometric evaluation of hemolysis in plasma by quantification of free oxyhemoglobin, methemoglobin, and methemalbumin in presence of bilirubin, J. Biophot. 14 (5) (2021), e202000461, https://doi.org/10.1002/jbio.202000461.
[61] F.D. Martínez-Mancera, J.L. Hernández-López, In vitro observation of direct electron transfer of human haemoglobin molecules on glass/tin-doped indium oxide electrodes, J. Mex. Chem. Soc. 59 (4) (2015) 302–307, https://doi.org/10.5772/67806.
[62] Y. Jin, D. Ni, L. Gao, X. Meng, Y. Lv, F. Han, H. Zhang, Y. Liu, Z. Yao, X. Feng, Harness the power of upconversion nanoparticles for spectral computed tomography diagnosis of osteosarcoma, Adv. Funct. Mater. 28 (33) (2018), 1802656, https://doi.org/10.1002/adfm.201802656.
[63] J. Raleigh, S. Chou, G. Arteel, M. Horsman, Comparisons among pimonidazole binding, oxygen electrode measurements, and radiation response in C3H mouse tumors, Radiat. Res. 151 (5) (1999) 580–589, https://doi.org/10.2307/3580034.
[64] X.-F. Li, S. Carlin, M. Urano, J. Russell, C.C. Ling, J.A. O'Donoghue, Visualization of hypoxia in microscopic tumors by immunofluorescent microscopy, Cancer Res. 67 (16) (2007) 7646–7653, https://doi.org/10.1158/0008-5472.CAN-06-4353.